

Physical and chemical conditions in methanol maser selected hot cores and UCH II regions

C. R. Purcell,^{1,2★} S. N. Longmore,^{2,3,4} M. G. Burton,² A. J. Walsh,^{2,5} V. Minier,^{2,6,7} M. R. Cunningham² and R. Balasubramanyam^{2,8}

¹University of Manchester, Jodrell Bank Observatory, Macclesfield, Cheshire SK11 9DL

²School of Physics, University of New South Wales, Sydney, NSW 2052, Australia

³Harvard-Smithsonian Center For Astrophysics, 60 Garden Street, Cambridge, MA 02138, USA

⁴CSIRO Australia Telescope National Facility, PO Box 76, Epping, NSW 1710, Australia

⁵Centre for Astronomy, James Cook University, Townsville, QLD 4811, Australia

⁶Service d'Astrophysique, DAPNIA/DSM/CEA Saclay, 91191 Gif-sur-Yvette, France

⁷AIM, Unité Mixte de Recherche, CEA–CNRS–Université Paris VII, UMR 7158, CEA/Saclay, 91191 Gif-sur-Yvette, France

⁸Raman Research Institute, Sadashivanagar, Bangalore 560 080, India

Accepted 2008 November 20. Received 2008 November 19; in original form 2008 October 18

ABSTRACT

We present the results of a targeted 3-mm spectral line survey towards the eighty-three 6.67 GHz methanol maser selected star-forming clumps observed by Purcell. In addition to the previously reported measurements of HCO^+ (1–0), H^{13}CO^+ (1–0) and CH_3CN (5–4) and (6–5), we used the Mopra antenna to detect emission lines of N_2H^+ (1–0), HCN (1–0) and HNC (1–0) towards 82/83 clumps (99 per cent), and CH_3OH (2–1) towards 78/83 clumps (94 per cent).

The molecular line data have been used to derive virial and local thermodynamic equilibrium masses, rotational temperatures and chemical abundances in the clumps, and these properties have been compared between subsamples associated with different indicators of evolution. The greatest differences are found between clumps associated with 8.6 GHz radio emission, indicating the presence of an Ultra-Compact H II (UCH II) region, and ‘isolated’ masers (without associated radio emission), and between clumps exhibiting CH_3CN emission and those without. In particular, thermal CH_3OH is found to be brighter and more abundant in UCH II regions and in sources with detected CH_3CN , and may constitute a crude molecular clock in single dish observations.

Clumps associated with 8.6 GHz radio emission tend to be more massive *and* more luminous than clumps without radio emission. This is likely because the most massive clumps evolve so rapidly that a Hyper-Compact H II or UCH II region is the first visible tracer of star formation.

The gas mass to submm/infrared luminosity relation for the combined sample was found to be $L \propto M^{0.68}$, considerably shallower than expected for massive main-sequence stars. This implies that the mass of the clumps is comparable to, or greater than, the mass of the stellar content.

We also find that the mass of the hot core is correlated with the mass of the clump in which it is embedded.

Key words: surveys – stars: formation – stars: pre-main-sequence – ISM: abundances – ISM: molecules.

1 INTRODUCTION

Molecular emission is a powerful tool when used to investigate the physical and chemical conditions in hot cores. Transitions requiring

different temperatures and densities for excitation constitute an excellent probe of physical structure. Because the chemical properties of hot cores vary with time, the relative molecular abundances can also be used as indicators of evolution.

In the preceding decades, representative line surveys of a limited sample of cores have begun to identify the molecules most suited to investigating the process of massive star formation. To

★E-mail: Cormac.Purcell@manchester.ac.uk

date, these have been restricted to a few objects: Orion-KL (Blake et al. 1986; Turner 1989; Ziurys & McGonagle 1993; Schilke et al. 1997), Sgr-B2 (Cummins, Linke & Thaddeus 1986; Turner 1989; Sutton et al. 1991), G34.3+0.15 (MacDonald et al. 1996; Kim et al. 2000, 2001), IRAS 17470–2853 (also known as G5.89–0.39, Kim, Balasubramanyam & Burton 2002) and G305.2+0.2 (Walsh & Burton 2006).

Chemical models, including both gas-phase and grain-surface reactions, have been developed for specific objects whose physical structure and conditions are well known, e.g. G34.3+0.15 (Millar, MacDonald & Gibb 1997; Thompson, MacDonald & Millar 1999), as well as for general cases, e.g. Rodgers & Charnley (2003). These and earlier models are limited by the computational power available at the time and consider either time-dependent chemistry at a test position or a ‘snapshot’ of spatial abundances at a single time. Advances in computational power have recently allowed the development of models which consider both time- and space-dependent chemistry simultaneously, e.g. the model of AFGL 2591 by Doty et al. (2002). Today it is the lack of observational constraints which restrict our understanding of chemistry in young massive stellar objects. The priority in the coming years must be to assemble a large sample of molecular abundance measurements towards a broad range of massive star-forming regions, at different stages of evolution and with luminosities and masses from B3 to O5 type massive stars.

In this paper, we present the remaining results of the Mopra ‘Hot Molecular Cores’ (HMC) survey towards 6.67 GHz methanol (CH_3OH) maser selected targets. The initial results were presented in Purcell (2006, hereafter Paper 1), wherein we reported the detection of the hot-core species methyl-cyanide (CH_3CN) and the observations of the formyl ion (HCO^+), and its isotopomer (H^{13}CO^+). Here, we expand the analysis to cover thermal transitions of methanol (CH_3OH), carbonmonoxide (^{13}CO), diazenylium (N_2H^+), hydrocyanic acid (HCN) and hydroisocyanic acid (HNC). We analyse the full complement of molecules for evidence of evolution.

Note: Tables S3–S9 are available in electronic form only along with additional supporting text and figures (see Appendix A).

2 OBSERVATIONS

Observations were conducted on the Mopra millimetre wave telescope over five years 2000–2004 during the winter observing season, June to September. We observed the transitions CH_3OH (2–1), ^{13}CO (1–0), N_2H^+ (1–0), HCN (1–0) and HNC (1–0) as single pointings, targeted at the maser sites. Electronic properties of the molecules and transitions are presented in Table 1. Five sources do not contain methanol masers but were detected as discrete clumps at 1.2 mm, adjacent to clumps containing CH_3OH masers (Hill et al. 2005). These ‘mm-only’ sources were observed as potential precursors to the hot-core phase of massive star formation. In each case, we targeted the peak of the 450 μm continuum emission later detected by Walsh et al. (2003). The signal from the receiver was processed in an autocorrelator back-end configured to have a bandwidth of 64 MHz, split into 1024 channels. At 3-mm wavelengths, this delivers a velocity resolution of $\sim 0.2 \text{ km s}^{-1}$ over a usable velocity interval of $\sim 130 \text{ km s}^{-1}$.

All observations were performed in a position switching mode by integrating for equal times on the science object and an emission-free reference position. Initial reduction of the raw data was per-

Table 1. Details of observed transitions.

Species	Transition	Frequency (GHz)	E_u/k^* (K)	A_{ul} (s^{-1})	g_u
$\text{CH}_3\text{OH}^\alpha$	$2_{(-1,2)} \rightarrow 1_{(-1,1)} \text{ E}$	96.739 390	4.642	2.495×10^{-6}	5
	$2_{(0,2)} \rightarrow 1_{(0,1)} \text{ A+}$	96.741 420	6.963	3.327×10^{-6}	5
	$2_{(0,2)} \rightarrow 1_{(0,1)} \text{ E}$	96.744 580	12.188	3.327×10^{-6}	5
	$2_{(1,1)} \rightarrow 1_{(1,0)} \text{ E}$	96.755 510	20.108	2.496×10^{-6}	5
$^{13}\text{CO}^\beta$	$1 \rightarrow 0$	110.210 353	5.288	6.389×10^{-8}	3
HNC^β	$1 \rightarrow 0$	90.663 593	4.350	2.709×10^{-5}	3
HCN^γ	$1_1 \rightarrow 0_1$	88.630 416	4.253	2.444×10^{-5}	3
	$1_2 \rightarrow 0_1$	88.631 847	–	–	5
	$1_0 \rightarrow 0_1$	88.633 936	–	–	1
$\text{N}_2\text{H}^+ \gamma$	$1_1 \rightarrow 0_1$	93.171 880	4.471	3.654×10^{-5}	9
	$1_2 \rightarrow 0_1$	93.173 700	–	–	15
	$1_0 \rightarrow 0_1$	93.176 130	–	–	3

$^\alpha J_{K,K_1} \rightarrow J'_{K',K'_1}$ quantum numbers.

$^\beta J \rightarrow J'$ quantum numbers.

$^\gamma J_F \rightarrow J'_{F'}$ quantum numbers.

* Energies of the upper levels relative to the $J_K = 1_{-1}$ level for E-type CH_3OH and relative to the $J_K = 0_0$ level for A-type CH_3OH .

formed using the *spc*¹ package. Polynomial baselines were subtracted from the line-free channels using the *xs*² software package. The *CLASS*³ spectral line analysis software was used for all further processing and analysis, including baseline subtraction and fitting Gaussian line profiles. For further details on the observing setup and data analysis, please refer to section 3 of Paper 1.

3 RESULTS

Thermal molecular emission was detected in 82/83 targets, with the exception being the source G10.10–0.72. In the interim period, this source has been reobserved at 6.67 GHz using the 30-m Ceduna radio telescope (University of Tasmania) and no CH_3OH maser was detected (Ellingsen, private communication). This source is thus most likely a noise artefact in the Walsh et al. (1998) survey and is discounted in the remainder of this work. Emission from ^{13}CO (1–0), N_2H^+ (1–0), HNC (1–0) and HCN (1–0) was detected towards the remaining 82 sources, while CH_3OH (2–1) emission was detected towards 79/82 sources (96 per cent). The 3σ noise limit on the spectra where no lines were detected is recorded in Table 2. Fig. 1 presents sample spectra for the source G323.74–0.26. The vertical dashed line marks the systemic velocity of the gas, measured from the optically thin H^{13}CO^+ line (Paper 1). In the case of CH_3OH , the rest frame is centred on the A+ transition; and for N_2H^+ and HCN, the rest frame is centred on the $J_F = 1_2 \rightarrow 0_1 \text{ E}$ transition. Plots of all molecular spectra for all 83 observed sources (including G10.10–0.72) are available as additional online material (see Appendix A).

3.1 Line profile parameters

As with CH_3CN in Paper 1, we fit the multiple transitions of CH_3OH (2–1) simultaneously with four Gaussian lines having equal

¹ *spc* is a spectral line reduction package for single dish telescopes written by the ATNF. <http://www.atnf.csiro.au/software/>

² *xs* is written by P. Bergman, Onsala Space Observatory. <ftp://yggdrasil.oso.chalmers.se/pub/xs/>

³ *CLASS* is part of the Grenoble Image and Line Data Analysis Software (GILDAS) working group software. <http://www.iram.fr/IRAMFR/GILDAS/>

Table 2. Noise detection limit on the spectra with no emission.

Source	CH ₃ OH	T_{MB} 3 σ detection limit (mK) ¹³ CO	N ₂ H ⁺	HNC	HCN
G0.32–0.20	230	–	–	–	–
G6.61–0.08	104	–	–	–	–
G10.10–0.72 ^a	69	414	142	127	163
G30.78+0.23	95	–	–	–	–

^aWalsh et al. (1997) originally detected a 6.67 GHz methanol towards G10.10–0.72. Subsequent observations (Ellingsen, private communication) have failed to detect the maser emission, hence we discard the source from our sample in the remainder of this work.

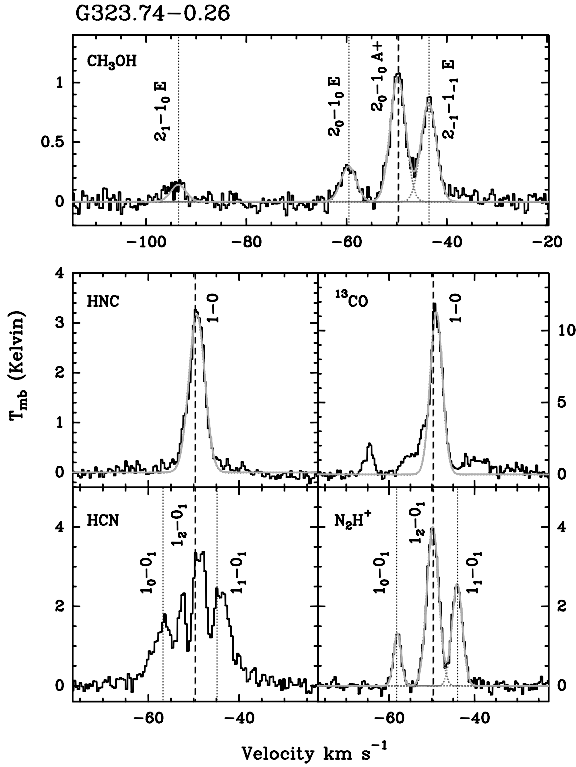


Figure 1. Sample spectra for the maser site associated with G323.74–0.26. The vertical dashed line marks the systemic velocity of the source, measured from the peak of the optically thin H¹³CO⁺ line profile (see Purcell 2006). Vertical dotted lines mark the expected velocity of other transitions of the same molecule. Individual Gaussian fits to the line profiles are plotted by a dotted grey line and the cumulative fit by a solid grey line. We did not attempt to fit Gaussian to HCN lines as the majority of profiles have complex shapes.

full width at half-maximum (FWHM) linewidths and whose line-centre separations were fixed to the theoretical values. The weakest component in the spectrum, the $J_{K',K''=2_{1,1} \rightarrow 1_{1,0}}$ E line, was detected towards 50 per cent of sources. Individual line profiles are generally well fit by single Gaussian, and the average linewidth is 4.7 km s^{-1} . The CH₃OH line profiles of five sources (G0.21+0.00, G0.26+0.01, G6.54–0.11, G10.30–0.15 and G15.03–0.71) were too confused or too weak to be successfully fit with Gaussian. The parameters of the Gaussian fits to the remaining 74 spectra are presented in Table S3.

The N₂H⁺ (1–0) transition is split into seven hyperfine lines as illustrated in Fig. 2 (adapted from Caselli, Myers & Thaddeus 1995).

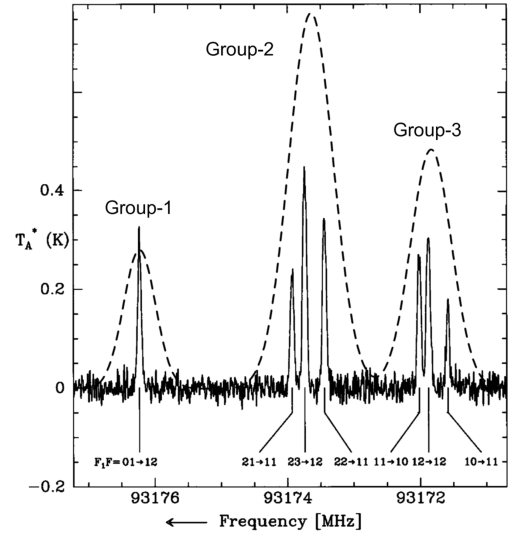


Figure 2. Spectrum of N₂H⁺ (1–0) towards a dark cloud showing the seven hyperfine components (Caselli et al. 1995). Linewidths towards massive star-forming regions are four to five times greater, resulting in the hyperfine components blending into three groups, designated 1–3 in this work (dashed lines).

The relatively broad linewidths ($>2 \text{ km s}^{-1}$) observed towards massive star-forming regions result in the seven components blending into three groups with roughly Gaussian shapes. Consequently, we have characterized the profiles using two analysis schemes. In the first instance, we used the hyperfine structure fitting (HFS) routine in the CLASS software to simultaneously fit the N₂H⁺ profiles with seven Gaussian. Free parameters were the velocity (V_{LSR}), common linewidth, excitation temperature and optical depth. In the case of severely blended lines (as presented in this work), the fits are not well constrained and values for the optical depth and excitation temperature contain substantial uncertainties. Using this method, we find the mean N₂H⁺ linewidth of the sample is 3.0 km s^{-1} . Because of the uncertainty introduced by the blending, CLASS assigned an erroneous value of $\tau = 0.1$ to all sources, rendering the resultant excitation temperatures meaningless. As an alternative measure of optical depth and integrated intensity, we also fit the three blended groups individually with single Gaussian. In total, we successfully fit Gaussian to 79 spectra. The N₂H⁺ emission in the source G0.26+0.01, G6.54–0.11 and G6.61–0.8 was too weak or too confused to achieve a reliable fit. We discuss the optical depth and column densities derived from the N₂H⁺ spectra in Section 4.4. The results of the CLASS HFS fits and the parameters of the Gaussian fits are presented in Table S4.

Line profiles of HNC are observed to be similar to HCO⁺. The critical densities of the two molecules are approximately the same at $\sim 3 \times 10^5 \text{ cm}^{-3}$ (Schilke et al. 1992) and it is likely that they trace the same gas. Both molecules exhibit high-velocity line wings. Self-absorbed HNC line profiles are common in the sample and we referred to the low optical depth H¹³CO⁺ and N₂H⁺ line profiles when attempting to distinguish between self-absorption and multiple clouds along the line of sight. We fit self-absorbed profiles with a single Gaussian by masking off the absorption dip (see Paper 1; Fig. 3). We also measured the line intensity by integrating under the line between velocity limits bracketing the positive line emission and we calculated an equivalent linewidth from

$$\Delta V_{\text{equiv}} = \frac{\int T_{\text{mb}} dv}{T_{\text{mb}}} \quad (1)$$

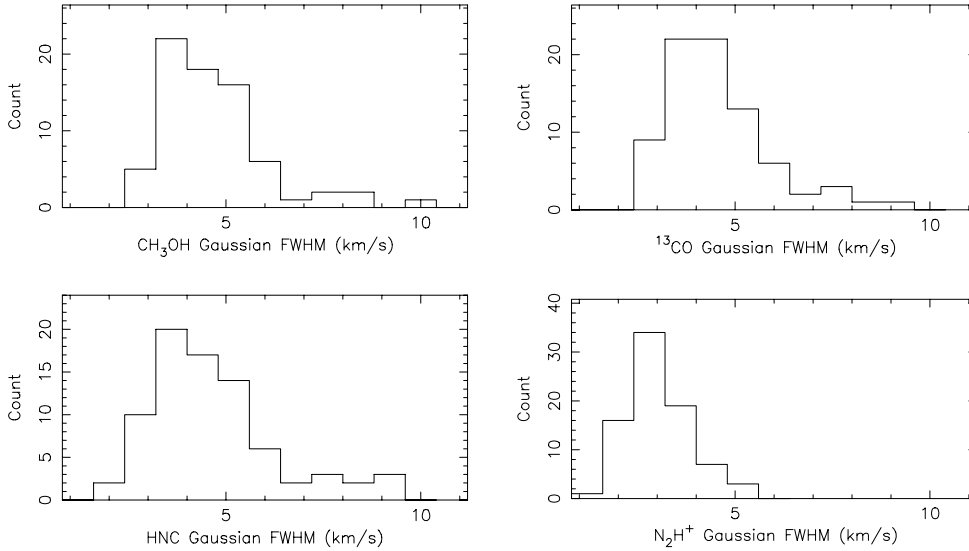


Figure 3. Distributions of FWHM linewidths from the Gaussian fits to the spectra. The HNC and ¹³CO line profiles were fit with single Gaussian components. CH₃OH was fit with multiple Gaussian, where the linewidths were constrained to have the same value. The N₂H⁺ spectrum was fit using the HFS method in CLASS. Seven Gaussian components with a common linewidth were fit to the three groups of blended lines. The value plotted here is the linewidth of an individual component. The mean CH₃OH, HNC and ¹³CO linewidth are all at approximately 4.5 km s⁻¹, while the mean N₂H⁺ linewidth is at 3.0 km s⁻¹.

In equation (1), $\int T_{\text{mb}} dv$ is the integrated intensity and T_{mb} is the peak main-beam brightness temperature. An HNC emission from the sources G0.21+0.00 and G0.26+0.01 was not measured as the line profiles were too confused. In total, 79 spectra were successfully fit with Gaussian, while 80 were measured by integrating under the line profile. The results of the fits and integrated intensity measurements are presented in Table S5.

The ¹³CO line profiles often exhibit multiple components spread over the 64 MHz bandpass. Usually, a single bright component is present at the systemic velocity of the source, which is easily fit with a single Gaussian. Occasionally, several smaller components are crowded around the main line and these are fit as blended Gaussian lines. In general, the ¹³CO profiles appear moderately optically thick but exhibit less self-absorption than HNC or HCO⁺. We again measure the integrated intensity and peak brightness temperature directly from the raw spectrum. The parameters of the fits and integrated intensity measurement of all 82 spectra are presented in Table S6.

HNC exhibited highly confused line profiles, with few sources exhibiting the expected three-component hyperfine structure. We attribute the complex profiles to a combination of high optical depths, multiple clouds along the line of sight and low level emission from broad-line wings tracing outflows. It is possible that some spectra may be contaminated by emission from the reference position, as HCN appears to be ubiquitous near the Galactic plane.

Like HCO⁺, high-velocity outflow wings are common in the spectra of HNC and, to a lesser extent, ¹³CO. We fit broad Gaussian to these wings simultaneously with the main component, and their parameters are presented in Tables S5 and S6 marked with a ‘w’. The Gaussian parameters for blended lines are marked with a ‘b’ in the same tables.

3.2 Linewidths

Fig. 3 shows the distributions of FWHM linewidths for the four molecules which were fit with Gaussian. The median CH₃OH, HNC and ¹³CO linewidths are all at approximately 4.5 km s⁻¹,

while the median N₂H⁺ linewidth is uniformly lower at 3.0 km s⁻¹. Kolmogorov–Smirnov (KS) tests yield probabilities above 50 per cent that the CH₃OH, HNC and ¹³CO linewidth distributions are similar, implying that these lines are emitted from gas with similar dynamics. In contrast, the N₂H⁺ distribution is significantly different, yielding probabilities of less than 0.0001 per cent in each case.

For a temperature of 58 K (see Section 4.1), the median intrinsic thermal linewidths for the molecules are as follows: CH₃OH: 0.29 km s⁻¹, ¹³CO: 0.31 km s⁻¹, HNC: 0.32 km s⁻¹ and N₂H⁺: 0.31 km s⁻¹. These values represent only 7 to 10 per cent of the measured linewidths. A non-thermal line broadening may arise from bulk motions, rotation or turbulence, which are difficult to distinguish at the resolutions of these observations. We can conclude that the N₂H⁺ emission emanates from a more quiescent region than the other molecules.

4 DERIVED PARAMETERS

We present the general physical parameters of the sources and the excitation temperatures, column densities and optical depths derived from the line profiles. The frequencies and electronic constants used in the calculations are collected in Table 1.

4.1 Gas mass and virial mass

Gas masses have been calculated from the 1.2-mm continuum flux density, taken from the work of Hill et al. (2005). For a 1.2-mm integrated continuum flux density, S_ν the mass of gas is given by Hildebrand (1983):

$$M_{\text{gas}} = \frac{S_\nu D^2}{\kappa_d R_d B_\nu(T_{\text{dust}})}, \quad (2)$$

where D is the distance to the source in metres, κ_d is the mass absorption coefficient per unit mass of dust, B_ν is the Planck function for a blackbody of temperature T_{dust} and R_d is the dust to gas mass ratio. We have adopted a value of 0.1 m² kg⁻¹ for κ_d at 1.2 mm and

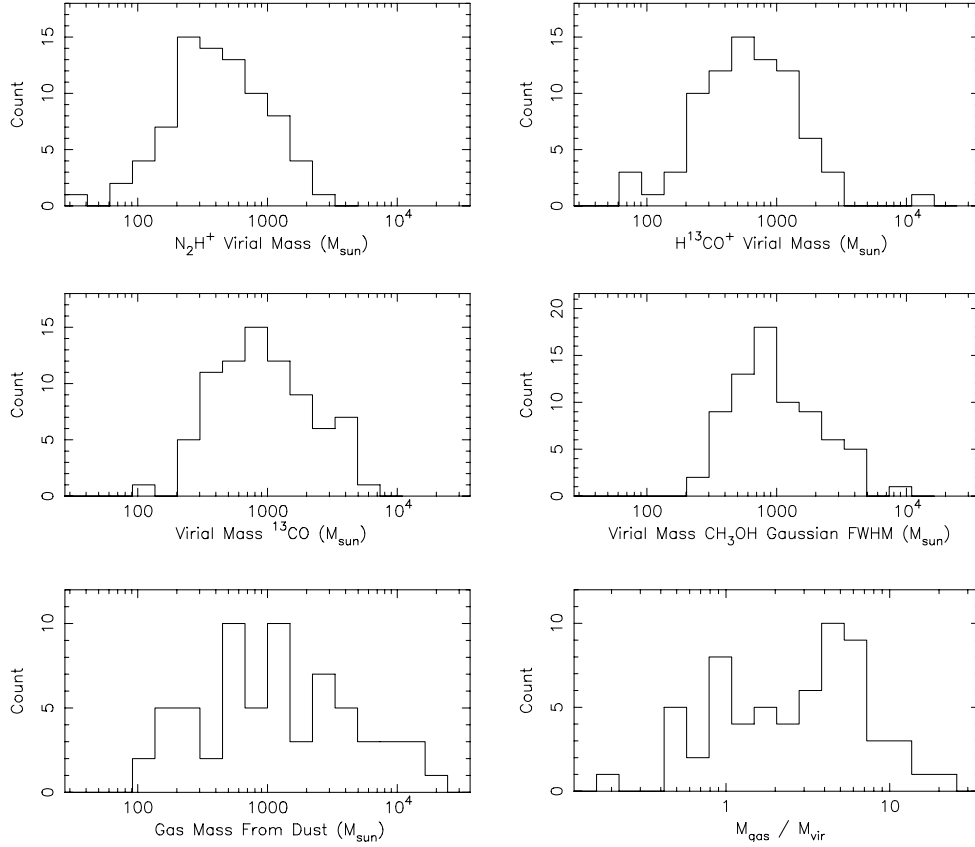


Figure 4. Histograms showing the distributions of the virial masses derived from N_2H^+ , H^{13}CO^+ , ^{13}CO and CH_3OH , and the gas masses derived from the 1.2-mm continuum emission from the work of Hill et al. (2005). Virial masses should be considered upper limits. The plot on the bottom right-hand panel shows the distribution of the $M_{\text{gas}}/M_{\text{vir}}$ ratio derived from N_2H^+ . The values of M_{gas} and M_{vir} are consistent with having the same order of magnitude, however, $M_{\text{vir}, \text{N}_2\text{H}^+} < M_{\text{vir}, \text{others}}$ as $\Delta v_{\text{N}_2\text{H}^+} < \Delta v_{\text{others}}$.

assumed a dust to gas mass ratio of 0.01 (Ossenkopf & Henning 1994). The distance has been estimated from the V_{LSR} of the source using the Galactic rotation curve of Brand & Blitz (1993) (see Paper 1). Values for T_{dust} were taken from the cold component of the grey body fit to the spectral energy distribution (SED) presented in Paper 1. For sources where we had insufficient data to perform a fit, we adopted the average value of $T_{\text{dust}} = 58$ K, determined from 65 good fits. We note that these temperatures are not well constrained by the sparsely sampled SED and are generally higher than the values of 20 to 30 K adopted in the literature. For dust temperatures of 20 and 30 K, the gas mass derived here will be underestimated on average by factors of 3.6 and 2.1, respectively. Values for M_{gas} were derived for 66 sources and are recorded in column six of Table S7.

We estimated virial masses from the CH_3OH , N_2H^+ , ^{13}CO and HNC line profiles following the approach by MacLaren, Richardson & Wolfendale (1988). In the simplest case, neglecting support by magnetic fields or internal heating sources, the total mass of a simple spherical system is given by

$$M_{\text{vir}} = \frac{\sigma^2 r}{G} = 126 r \Delta v^2 \quad \dots \quad \text{in } (M_{\odot}), \quad (3)$$

where σ is the full three-dimensional velocity dispersion, r is the dust-radius of the cloud in pc, Δv is the FWHM linewidth of the molecular line in km s^{-1} and G is the gravitational constant in $\text{m}^3 \text{kg}^{-1} \text{s}^{-2}$. The virial mass is the minimum mass required in order for a cloud to be gravitationally bound, i.e. the cloud is bound if

$M_{\text{gas}}/M_{\text{vir}} > 1$. If magnetic field support is important, the virial mass may be overestimated by up to a factor of 2 (MacLaren et al. 1988). Observationally, the linewidths may be artificially broadened due to the blending of multiple components along the line of sight, or in optically thick lines, due to radiative transfer effects. Enhanced linewidths will cause us to overestimate the virial mass by an unknown amount and the values quoted here should be considered upper limits. Columns 7–10 of Table S7 present the virial masses derived from the four molecules.

The distributions of M_{gas} and M_{vir} are illustrated in Fig. 4. Optically thin N_2H^+ and H^{13}CO^+ produce similar estimates of the mean virial mass at 573 and 905 M_{\odot} , respectively. ^{13}CO and CH_3OH have the broadest linewidths, most likely due to optical depth effects or low-velocity outflows, leading to mean mass estimates of 1293 and 1305 M_{\odot} , respectively. The values derived for M_{gas} and M_{vir} are consistent with having the same magnitude in the majority of clumps. The large uncertainties associated with the calculations prevent the interpretation of individual objects as gravitationally bound.

4.2 H_2 column and volume density

We estimated the H_2 column density, N_{H_2} , from the gas mass using the following relation:

$$N_{\text{H}_2} = \frac{M_{\text{gas}}}{2 M_{\text{p}} f_{\text{He}} A}, \quad (4)$$

where $M_p = 1.673 \times 10^{-27}$ kg is the mass of a proton, $f_{\text{He}} = 1.36$ is a correction factor to account for Helium present in the interstellar medium (Allen 1973) and A is the projected surface area of the mm-continuum emission. Assuming a cylindrical source with a uniform density, the projected area is given by

$$A = \pi r^2 D^2, \quad (5)$$

where r is the angular radius of the source in radians and D is the distance to the source in metres ($1 \text{ pc} = 3.08568 \times 10^{16} \text{ m}$). In a similar manner, the volume density n_{H_2} can be estimated by replacing A in equation (4) by V the projected volume of emitting gas

$$V = \frac{4}{3} \pi r^3 D^3. \quad (6)$$

Equation (6) assumes emission from a uniformly dense sphere of angular radius r . The radius of the dust continuum emission was measured directly from the 1.2-mm continuum images (provided courtesy of Hill et al. 2005) by fitting a Gaussian to the azimuthally averaged source profiles. We find values for the FWHM vary between 99 and 24 arcsec (the limiting resolution of the SIMBA bolometer), and have a mean value of 34 arcsec. Derived values of N_{H_2} and n_{H_2} are presented in columns four and five of Table S7 and have means of 6.1×10^{22} and $4.8 \times 10^4 \text{ cm}^{-3}$, respectively.

We urge caution in interpreting any value of the H_2 column density derived in this manner as the assumptions introduce large unknown errors. First, the mass absorption coefficient and dust to gas ratio used to calculate M_{gas} in equation (2) may vary considerably from source to source, leading to a corresponding error in the H_2 column density. The spatial distribution of H_2 is further unknown and additional errors are introduced by assuming a uniform column density over a spherical projected volume. For the six sources at the limit of SIMBA resolution (24 arcsec) derived values should be considered beam-averaged lower limits. Also see Section 6.3 for a discussion on beam dilution.

4.3 CH_3OH rotational temperature and column density

CH_3OH is a slightly asymmetric rotor, resembling a symmetric top except for the O–H group, which is angled with respect to the principal axis. Internal hindered motion coupled with the rotation

of the molecule results in a complicated rotational spectrum, organized into non-degenerate A and two-fold degenerate E levels, corresponding to different torsional symmetry. The A and E states have nuclear statistical weights of 2 and 1, respectively, thus their overall degeneracy is the same (Bockelee-Morvan et al. 1994).

A rotational temperature T_{rot} and column density N may be estimated from the ratios of the thermal CH_3OH lines based on the assumptions of low optical depths and that the background temperature ($T_b \approx 2.7 \text{ K}$) is small compared to the brightness temperature of the line. Under conditions of local thermodynamic equilibrium (LTE), all the observed energy levels can be described by a single excitation temperature T_{ex} , defined by the Boltzmann relation. Using the relation for rotational temperature (Goldsmith & Langer 1999),

$$\ln \left(\frac{N_u}{g_u} \right) = \ln \left[\frac{N}{Q(T)} \right] - \frac{E_u}{k T_{\text{rot}}} \quad (7)$$

a rotation diagram may be drawn by plotting $\ln(N_u/g_u)$ versus E_u/k . The rotation temperature and column density in the upper level N_u are found from the slope and y-axis intercept, respectively, of a straight line fit to the data. The total column density N may then be found assuming LTE and a partition function $Q(T_{\text{rot}})$, which for CH_3OH is given by (Townes & Schawlow 1955)

$$Q(T) = \sum_{J=0}^{\infty} (2J+1) e^{-E_J/kT} \approx 1.2327 T_{\text{rot}}^{1.5}. \quad (8)$$

In equation (8), we have approximated the partition function by a fit to the discrete values in the Pickett et al. (1998) spectral line catalogue. Note that values for E_u are referenced to different ground-state energy levels in A- and E-type CH_3OH . The ground state for A-type is the $J_K = 0_0$ level, while for E-type CH_3OH is the $J_K = 1_{-1}$ level (Menten et al. 1988). This is commonly overlooked in the literature as all values quoted in Pickett et al. (1998) are referenced to the $J_K = 0_0$ level, resulting in incorrect rotation diagrams. The correct values of E_u/k are cited in Table 1.

An example of a CH_3OH rotation diagram is shown in Fig. 5 (left-hand panel). The data point at $E_u/k \approx 7 \text{ K}$ corresponds to the A+ line, while the other three points correspond to E transitions. In general, where we detect three E-type lines, they are well fit with a straight line, implying that our assumption of optically thin conditions is valid.

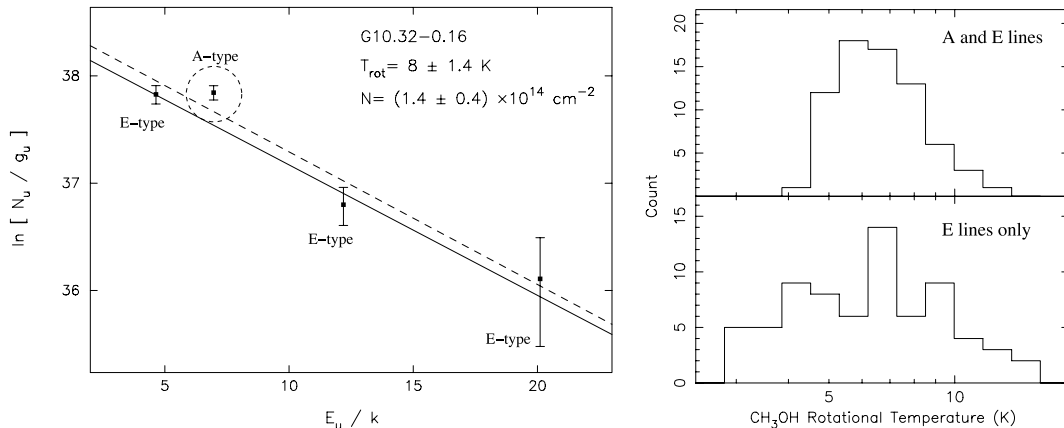


Figure 5. Left-hand panel: rotational diagram of CH_3OH for the source G10.32–0.16, made using the 96.7 GHz lines. The point at $E_u \approx 7 \text{ K}$ corresponds to the $2_0 \rightarrow 1_0$ A+ transition. The three other points are due to transitions of E-type methanol. The solid line and values for T_{rot} and N correspond to a fit through the E transitions only. The dashed line represents a fit to all transitions. Right-hand panel: distributions of rotational temperatures derived from CH_3OH using both A- and E-type transitions (top panel) and E-type transitions only (bottom panel).

A and E type methanol are oblate and prolate forms, respectively, of the asymmetric top and only interconvert on time-scales of $\sim 10\,000$ yr. It is not clear that the A/E ratio can be assumed equal to 1 and a rotation diagram including both A and E type transitions may not be valid. In Fig. 5 (left-hand panel), the solid line indicates a fit to the E-type transitions only, while the dotted line is a fit to both the A and E type. Rotation temperatures derived from only the E-transitions have a mean value of 6.67 K, similar to the mean temperature derived from all four transitions, which is 6.8 K. Rotational temperatures and column densities derived using both fitting methods are presented in Table S8 and the distributions of rotational temperatures are illustrated in Fig. 5 (right-hand panel).

Column densities are averaged over the telescope beam and likely underestimated. If the bulk of the CH_3OH emission stems from within the bounds of a hot core then the typical size of the emitting region will be ~ 0.1 pc ($\approx 20\,000$ au, Kurtz et al. 2000). Columns three and four of Table S8 present the angular size and beam dilution factor calculated using this assumption. Columns seven and ten present the column densities corrected for this assumed dilution factor.

On inspection of the bulk of the rotation diagrams (available as an online supplement), we see a pattern emerge. The A-type transition has a consistently higher N_u/g_u compared to a straight line fit through the E-type transitions. This indicates a greater abundance of A-type CH_3OH and an A/E ratio > 1 . Considering only sources in which all three E-type lines were detected (36 sources), and assuming equal excitation temperatures in A and E lines, we derive A/E abundance ratios ranging from 0.47 to 1.80, with a mean of 1.30. These values are comparable to values previously derived in the literature, e.g. Menten et al. (1988) who calculated A/E ratios between 1.3 and 2.0, using the same transitions, towards warm clumps in Orion-KL.

4.4 N_2H^+ optical depth and column density

Optical depths were derived from the blended hyperfine components of N_2H^+ , which assume set ratios under optically thin conditions (see Section 3.1). Assuming the linewidths of the individual hyperfine components are all equal, the integrated intensities of the three blended groups should be in the ratio of 1 : 5 : 2 under optically thin conditions. The optical depth is calculated from the ratio of integrated intensities ($\int T_B dv$) of any two groups using the following equation:

$$\frac{\int T_{B,1} dv}{\int T_{B,2} dv} = \frac{1 - e^{-\tau_1}}{1 - e^{-\tau_2}} = \frac{1 - e^{-\tau_1}}{1 - e^{-a\tau_1}}, \quad (9)$$

where ‘ a ’ is the expected ratio of τ_2/τ_1 under optically thin conditions. Caselli et al. (1995) report anomalous excitation of the $F_1, F = 1, 0 \rightarrow 1, 1$ and $1, 2 \rightarrow 1, 2$ components (in our group 3), so we determine the optical depth solely from the intensity ratio of group 1/group 2. We find that 97 per cent of sources have optical depths below 1. Fig. 6 plots the distribution of the derived optical depths, which range from 0.035 to 2.43, with a mean of 0.35 and a standard deviation of 0.42. Values for the optical depth towards individual sources are presented in column two of Table S9.

Column densities of N_2H^+ can be found from the following standard formula (Rohlfs & Wilson 2004):

$$N = \frac{8\pi\nu^2}{A_{ul}hc^3} \int T_B dv \left(\frac{\tau_\nu}{1 - e^{-\tau_\nu}} \right) \frac{Q(T_{\text{ex}})}{g_u} e^{E_u/kT}, \quad (10)$$

where $Q(T_{\text{ex}})$ is the partition function, extrapolated from a fit to the

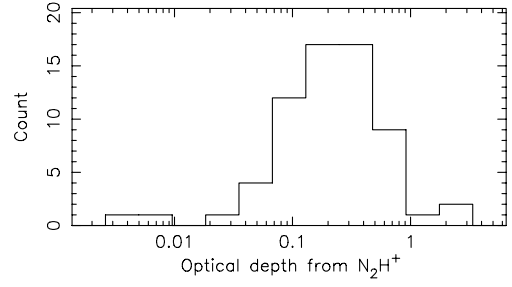


Figure 6. Distribution of optical-depths derived from the ratios of the hyperfine groups of N_2H^+ . The mean is 0.35 ± 0.42 .

values given by the (Pickett et al. 1998) spectral line catalogue:

$$Q(T) = 4.198 T_{\text{ex}}. \quad (11)$$

Equation (10) requires an estimate of the excitation temperature T_{ex} . Unfortunately, under optically thin conditions, the excitation temperature cannot be determined from the N_2H^+ line profiles, so we assume a constant value of 10 K. For excitation temperatures of 5 and 20 K, the total column density should be multiplied by 0.8 and 1.6, respectively. Beam-averaged column densities derived using equation (10) are presented in column five of Table S9. In the literature, high-resolution maps show that N_2H^+ traces the spatial extent of the dust closely (e.g. Caselli et al. 2002a; Pirogov et al. 2003). We have estimated the average FWHM of the dust emission for all sources observed by Hill et al. (2005) (see Section 4.2) and use these values to correct for beam dilution. Total column densities corrected by a factor of $(\theta_{\text{dust}}/\theta_{\text{beam}})^2$ are presented in column six of Table S9.

4.5 ^{13}CO , HNC and HCN column density

The HNC, HCN and ^{13}CO profiles frequently display asymmetries which may indicate that they are optically thick in general. Lacking an estimate for both the excitation temperature and the optical depth, we are unable to calculate reliable column densities.

4.6 Abundances

The relative abundance X between two species may be found directly from the ratio of their volume densities. Assuming both molecules occupy the same volume of space, this is simply equivalent to the ratio of their column densities:

$$X = \frac{n_1}{n_2} \approx \frac{N_1}{N_2}. \quad (12)$$

If, however, one or both species subtend angles smaller than the beam, we must correct for their *relative* volume filling factor and equation (12) becomes

$$X = \frac{N_1}{N_2} \left(\frac{\theta_2}{\theta_1} \right)^3, \quad (13)$$

assuming spherically symmetric emission with characteristic sizes θ_1 and θ_2 . For the single-position observations presented here, the volume filling factors are complete unknowns and constitute the greatest source of errors in the abundance. Additional errors stem from the calibration of the brightness scale (~ 30 per cent) and the pointing accuracy of the telescope (~ 20 per cent). Abundances relative to H_2 depend also on the assumptions made in calculating the gas mass from the 1.2-mm continuum emission and cannot be determined reliably.

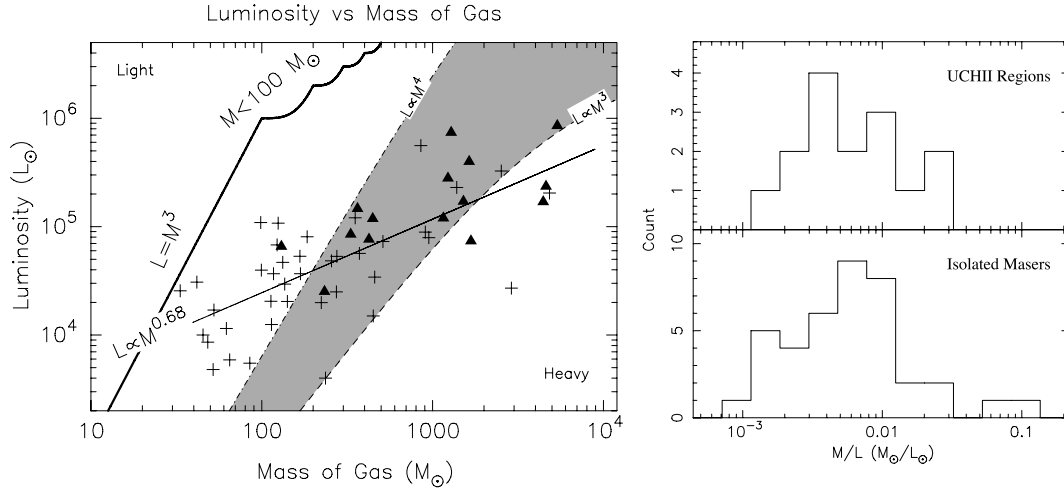


Figure 7. Left-hand panel: plot of luminosity versus dust + gas mass for 55 sources whose properties could be determined (after Fig. 2, Cesaroni 2005). UCH II regions are represented by solid triangles and isolated masers by crosses. The thick solid line traces the luminosity expected if $M_{\text{gas}} \equiv M_{\text{stars}}$ in the clumps, and the stellar population is concentrated in a minimum number of stars with masses $\leq 100 M_{\odot}$. The dashed line is the luminosity expected from the most massive star in a M_{gas} cluster with stellar masses distributed according to a Salpeter IMF ($\alpha = 2.35$), and a fundamental upper stellar mass limit of $150 M_{\odot}$ (Weidner & Kroupa 2004). We have assumed a mass–luminosity relation of $L \propto M^3$. The dash-dotted line traces the expected luminosity from the same IMF assuming $L \propto M^4$ and the shaded region indicates intermediate values. The observed mass–luminosity relation is fit with a single power law of index 0.68 ± 0.09 (thin solid line). Right-hand panel: histograms of the distribution in the $M_{\text{gas}}/L_{\text{stars}}$ values for UCH II regions and isolated masers. A KS test cannot distinguish between them.

5 LUMINOSITIES AND MASSES

The relationship between mass and luminosity provides clues to the star formation efficiency, stellar content and evolutionary state of the clumps. Fig. 7 (left-hand side) is an expanded version of fig. 2 in Cesaroni (2005), showing the relationship between luminosity and gas mass for the 55 clumps whose properties could be determined. The luminosity has been measured from a two-component grey body fit to the SED, and is directly related to the stellar content of the clump. Submillimetre emission from assumed optically thin dust (Hill et al. 2005) has been used to derive the total gas mass of the clumps. In the plot, the thick line marks the expected luminosity from a minimum number of stars of mass $M_* \leq 100 M_{\odot}$, assuming $M_{\text{gas}} \equiv M_{\text{stars}}$. Cesaroni (2005) divides a sample of 21 known hot cores⁴ into ‘light’ and ‘heavy’ categories, based on their position above or below this division. ‘Light’ cores have gas masses below $\sim 100 M_{\odot}$ and fall above the thick line. Their high luminosity-to-mass ratio implies that the mass of their stellar content is greater than that of the gas. ‘Heavy’ cores have gas masses above $\sim 100 M_{\odot}$ and fall below the thick line. The mass of their stellar content is comparable to, or less than, the mass of the gas. Cesaroni (2005) has interpreted the $L_{\text{stars}}/M_{\text{gas}}$ ratio in the ‘light’ cores as suggesting only a single embedded massive star exists in these clumps. Conversely, the ‘heavy’ clumps are likely to contain multiple massive stars which have formed in clustered mode. We do not find any ‘light’ cores in our sample.

An alternative explanation for high $L_{\text{stars}}/M_{\text{gas}}$ ratios in the ‘light’ sources might derive from the age of the star-forming regions. A massive young stellar object at a late stage of evolution could be expected to have dispersed a large fraction of its molecular gas, through the action of stellar winds, intense ultraviolet-radiation

(UV-radiation) and outflows from young OB stars. This would result in a decrease in the measured gas mass without a corresponding decrease in the luminosity. In Fig. 7, the points would move horizontally into the ‘light’ portion of the plot. We note that Cesaroni’s light cores include Orion-KL and IRAS 20126+4014, neither of which are believed to be at a late stage of evolution. Orion is the closest massive star-forming region and is not clear if it is a representative of massive star-forming regions in general. The mass of IRAS 20126+4014 ($7 \pm 3 M_{\odot}$) has been measured assuming Keplerian rotation of a molecular disc (Cesaroni et al. 2005) and relates to the inner object only. On larger scales, the gas mass has been measured to be several hundred solar masses (e.g. Estalella et al. 1993), putting IRAS 20126+4014 in the ‘heavy’ category. We find that all of our maser selected sample have gas masses above $\sim 30 M_{\odot}$ and *all* fall into the ‘heavy’ category. If the division between ‘light’ and ‘heavy’ cores is an indication of age, then all of our sample are at a relatively early stage of evolution, i.e. the powering massive young stellar objects have not yet dispersed their natal molecular clouds.

In Fig. 7, the shaded region between the dashed lines represents the range of luminosities expected from the *most massive* star in a cluster where $M_{\text{stars}} = M_{\text{gas}}$, if the initial mass function (IMF) follows a Salpeter power law ($\alpha = 2.35$) and assuming a fundamental upper stellar mass limit of $M_* = 150 M_{\odot}$ (Weidner & Kroupa 2004). The luminosity of the cluster will be dominated by the most massive star so this is a good approximation to the expected total luminosity. The range in expected luminosities derives from the uncertainty in the mass–luminosity relation for massive young stellar objects. This may be represented by a power law of the form $L_* \propto M_*^{\gamma}$, where γ ranges between 3 and 4 in the literature for OB stars (e.g. Lada 1999; Churchwell 2002). Our maser selected sample exhibits a rough correlation between mass and luminosity, which may be fit with a single power law with index $\gamma = 0.68 \pm 0.08$. This is a much shallower rise than observed in evolved stars, however, the luminosities of the most massive clusters are consistent with the

⁴ We have the following sources in common with Cesaroni: G5.89–0.39, G9.62+0.19, G10.47+0.03, G10.62–0.38, G29.96–0.02 and G31.41+0.31.

150 M_{\odot} stellar cut-off (Weidner & Kroupa 2004), even in the more conservative limit of $L_* \propto M_*^3$.

The derived gas mass is highly dependent on the temperature in equation (2). The shallow power law might be explained if the average dust temperature increases with luminosity and this change is not reflected in the sparsely sampled grey body fits to the SED, from which we take our temperature estimates. If we assume the mass estimates are correct to within a factor of a few, then the main result is that the lower mass clumps are overluminous and the higher mass clumps are underluminous.

5.1 UCH II regions: luminosity or age?

UCH II regions (triangles) are, in general, more luminous *and* more massive than the isolated masers (crosses) in the sample. Individual power-law fits to the isolated masers and UCH II subsamples yield mass–luminosity relations of $L_{\text{bol}}|_{\text{masers}} \propto M^{0.59 \pm 0.13}$ and $L_{\text{bol}}|_{\text{UCH II}} \propto M^{0.64 \pm 0.18}$, respectively. These fits are consistent with the fit to the combined sample, within the errors, and a single power law can describe both distributions. Fig. 7 (right-hand panel) is a histogram of the $M_{\text{gas}}/L_{\text{stars}}$ ratio for UCH II regions (top panel) and isolated masers (bottom panel). As expected from the mass–luminosity plot, the distributions are similar and a KS test cannot distinguish between them, yielding a 76 per cent probability of the two subsamples being drawn from the same population. This result implies that for the same masses, the two samples have the same luminosities. Early in the evolution of a massive young stellar object, we would expect its luminosity to increase as it accretes matter and more mass is transferred from the envelope to the star. At the same time, the overall mass of gas and dust in the clump is expected to remain relatively constant, or indeed decrease, as winds from the young OB cluster break up the cloud. By this rationale, if our sample of UCH II regions is older and more evolved, we would expect them to have a lower $M_{\text{gas}}/L_{\text{stars}}$ ratio than the isolated masers. There are several possible reasons why we do not see a difference between the mass–luminosity distributions.

It is possible that systematic errors (which we discuss below) associated with our assumptions cause us to overestimate the mass of the clouds hosting the UCH II regions relative to the clouds hosting the isolated masers. For there to be no difference between the mean masses of the subsamples, the isolated masers would need to have

a dust temperature on average 36 K lower than the UCH II regions. Fig. 8 (left-hand panel) illustrates the distributions of T_{cold} from the SED fits, for UCH II regions (top panel) and isolated masers (bottom panel). While the UCH II regions clearly have temperatures which are skewed to the high end, the difference in the means is only 4.3 K. The rotational temperatures calculated from CH_3CN are likewise similar, however, we cannot rule out different average dust temperatures on the basis that CH_3CN emission likely probes only the embedded ‘hot core’ and does not reflect the conditions in the extended clump. Thermal CH_3OH emission is thought to derive from a more extended envelope and rotational temperatures calculated from this molecule appear to support very different temperatures in the two groups. Fig. 8 (right-hand panel) shows histograms of the CH_3OH rotational temperature for the UCH II regions (top panel) and isolated masers (bottom panel). A KS test returns a probability of 0.002 per cent of the distributions deriving from the same parent. We note that the mean values of 9.9 K for the UCH II regions and 6.1 K for the isolated masers do not reflect the kinetic temperature as the CH_3OH is likely subthermally excited (see Goldsmith & Langer 1999).

As an alternate estimate of the mass, we derived an ‘LTE–mass’ from the column density of N_2H^+ . In our calculations, we assume (i) the N_2H^+ emission closely traces the 1.2-mm dust continuum and has a flat density distribution within the FWHM of the clump and (ii) a fixed $[\text{H}_2]/[\text{N}_2\text{H}^+]$ abundance ratio of 1.7×10^{-10} (Pirogov et al. 2003). The mass of gas may then be estimated from the column density using equation (4). Fig. 9 (left-hand panel) is a mass–luminosity plot similar to Fig. 7, except that the mass plotted on the x-axis is the LTE–mass calculated from N_2H^+ . Although the scatter is greater, we clearly see the masses of the UCH II regions and isolated masers are still weakly offset, with the UCH II regions having greater masses on average, as in Fig. 7. The distributions of the $M_{\text{gas}}/L_{\text{stars}}$ ratios are illustrated in Fig. 9 (right-hand panel). A KS test returns a probability of 50 per cent that both distributions are derived from the same parent, confirming the original result.

Another explanation for the offset in the masses derives from the sensitivity limit on the radio survey. In the preceding paper, we assumed the UCH II regions were older and more evolved than the isolated masers. We argued that the original radio continuum survey was sensitive enough to detect UCH II regions associated with the less luminous isolated masers (see Paper 1). However, if a

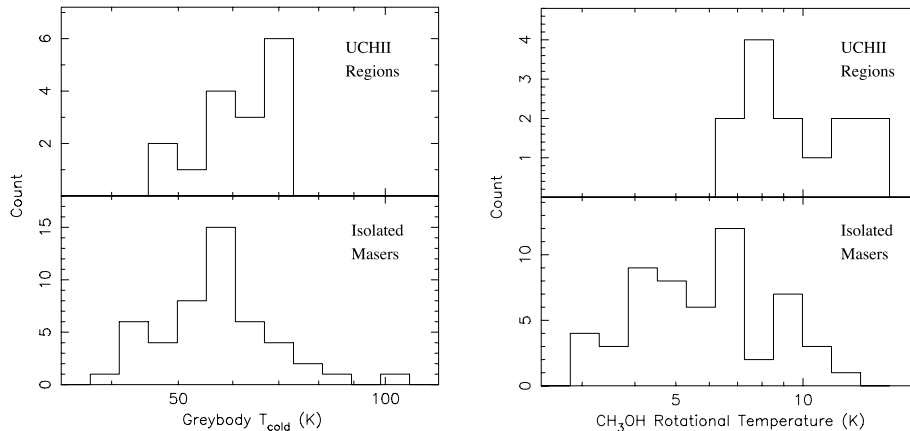


Figure 8. Left-hand panel: histograms showing the distributions of dust temperature taken from the cold component of the grey body fit to the SED. The top panel shows UCH II regions, which have a mean T_{cold} of 62.4 K, while the bottom panel shows isolated masers, which have a mean T_{cold} of 58.1 K. Right-hand panel: histograms showing the distributions of CH_3OH rotational temperature for UCH II regions (top panel) and isolated masers (bottom panel). The mean values are 9.9 K for UCH II regions and 6.1 K for isolated masers. A KS test establishes that the CH_3OH rotational temperature distributions are significantly different, returning a probability of 0.002 per cent.

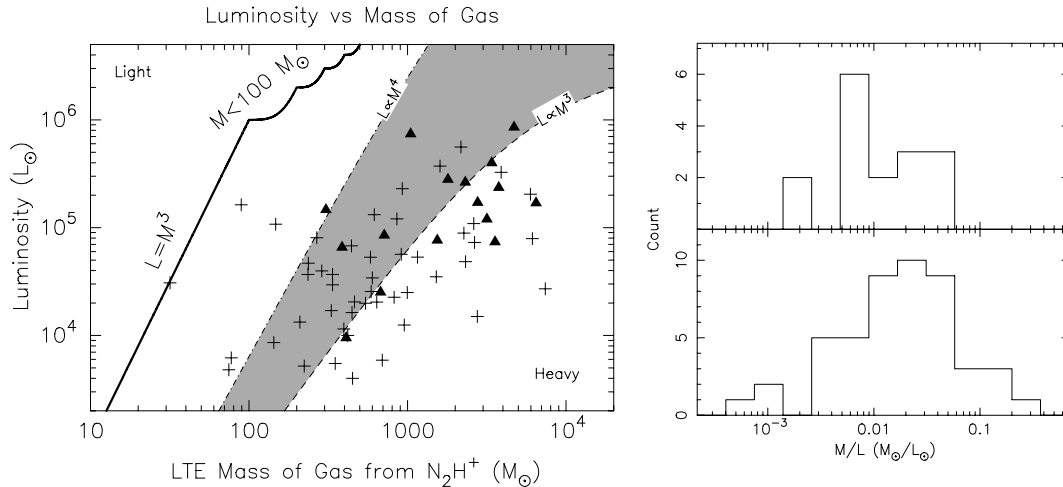


Figure 9. As Fig. 7, except in this case the mass is the LTE-mass derived from the column density of N_2H^+ assuming a fixed abundance ratio of 1.7×10^{-10} and that the N_2H^+ emission closely follows the spatial distribution of the 1.2-mm continuum emission.

sensitivity bias existed, it would manifest as a mass and luminosity offset between the radio loud and radio quiet, i.e. the UCH II regions would be *more massive and more luminous* than isolated masers. In other words, some of the lower L_{stars} isolated masers may indeed be associated with UCH II regions which fall below our detection limit. In Paper 1, we showed that most sources are luminous enough to have detectable UCH II regions, assuming up to 90 per cent of the Lyman continuum photons are absorbed by dust (Kurtz, Churchwell & Wood 1994). If the disparity in luminosity were due to a real sensitivity limit, this would imply that, on average, at least 99 per cent of the ionizing photons are absorbed by dust before contributing to the creation of a UCH II region. We believe this is unlikely in the majority of cases.

Some of the isolated maser sites may also be associated with Hyper-Compact H II (HCH II) regions. This recently discovered class of H II region is typically less than 0.01 pc across (Avalos et al. 2006) and exhibits a free-free emission spectrum with a turnover at higher frequencies than UCH II regions, typically 20 GHz. HCH II regions are expected to be optically thick at 8.6 GHz due to the squared dependence of the flux density with frequency and will be difficult to detect. Longmore et al. (2007) had used the Australia Telescope Compact Array to search for 22 GHz emission towards 24 of the objects presented here. Nine of these sources fall into the radio-quiet category and of these seven exhibit compact ($30 \rightarrow 3$ arcsec) continuum emission. This result strongly suggests that some of our radio-quiet sources are associated with HCH II regions, or indeed UCH II regions undetected at 8.6 GHz. However, because HCH II regions are thought to be the precursors of UCH II regions, we are still selecting for two different evolutionary states.

The most obvious explanation for the offset is due to the time-scales on which we expect massive young stellar objects to progress to develop a detectable UCH II region. In essence, clumps containing very high mass objects will evolve very rapidly and will spend only a short time in hot core and earlier phases. Because of the short time-scales involved, very massive hot cores will also likely be deeply embedded. The first indication of star formation activity may be when the expanding H II region begins to disperse the surrounding molecular gas. Anecdotal evidence supporting this explanation is already emerging from uniform searches for massive young stellar objects (MYSOs), such as the Red MSX Source (RMS) survey (Hoare et al. 2004; Mottram 2008). The less evolved MYSOs iden-

tified in the survey have a significantly smaller upper mass cut-off compared to the UCH II regions detected. No MYSO counterparts are found to the most massive UCH II regions, implying that the UCH II phase is the first indication of star formation in the most massive clumps.

We believe differences between the radio-bright and radio-quiet samples may be attributed to evolution, with the caveat that the highest luminosity objects do not spend significant time in an ‘isolated maser’ phase.

6 DETAILED COMPARISON BETWEEN SUB-SAMPLES

The aim of this molecular survey is to investigate the utility of molecular lines in the 3-mm band to act as ‘molecular clocks’. In this section, we consider the differences between subsamples divided from the source list based on associations with tracers of potentially different evolutionary states.

In Paper 1, we examined the link between hot cores, 6.67 GHz CH_3OH masers and UCH II regions. We found that CH_3CN was brighter and more commonly detected towards masers associated with UCH II regions, than towards ‘isolated’ masers. Asymmetries in the HCO^+ versus H^{13}CO^+ line profiles were interpreted as inward (blue skewed) or outward (red skewed) gas motions. We also examined the associations with mid-infrared (mid-IR) emission in the Midcourse Space Experiment (MSX) images and found 11 dark clouds (seen in absorption against the $8 \mu\text{m}$ Galactic background) and 67 in emission. Many of the sources also exhibited high-velocity line wings, indicative of outflows. Based on these results, we separate the source list into subsamples based on the following criteria.

- (i) Presence or absence of radio emission from a UCH II region.
- (ii) CH_3CN detected versus no CH_3CN detected.
- (iii) MSX dark (seen in absorption at $8 \mu\text{m}$) versus MSX bright.
- (iv) Presence or absence of high-velocity line wings in HCO^+ , HNC or ^{13}CO .
- (v) Presence or absence of blue-skewed HCO^+ line profiles, indicating infall.

In the following analysis, we contrast the subsamples by looking for differences in the median properties. A KS test is used to assess the similarity of the two distributions and trends are found

based on large differences in the median values, coupled with a low probability that the subpopulations are drawn from the same parent distribution.

Initially, we compare the spectral line luminosities calculated from the integrated line intensity multiplied by the square of the distance to the source. If the distance is well known then comparisons of line luminosities will potentially reveal intrinsic differences between the subsamples. However, the error in the distance for this sample is relatively large (± 0.65 kpc ≈ 20 per cent), and increases drastically towards Galactic longitudes $< 5^\circ$, where the model Galactic rotation curve begins to break down. Only the strongest trends will be seen using such a comparison.

We also compare the distance-independent linewidths. Linewidths in massive star-forming regions are generally much greater than the thermal width and are indicators of the level of turbulence present in the gas. Turbulence arises from bulk motions of gas, is often associated with energetic phenomena, such as outflows, and is correlated with star formation activity (e.g. Dobbs, Bonnell & Clark 2005).

The ratio of two spectral line intensities is unaffected by the distance and constitutes a much better probe of the physical and chemical conditions. The dominant errors are due to the relative accuracy with which the data have been calibrated and the unknown beam filling factors. The results presented here are based on data taken over four years and the calibration error in the data has been determined to be better than 30 per cent in most cases. The uncertainty due to the beam filling factors is given by the ratio of the solid angles over which the two molecules emit, (Ω_1/Ω_2), and may be large for dense-gas tracers which subtend angles smaller than the beam. The trends underlying the data should still be visible given the sample size.

Ideally, in a search for molecular clocks, the abundances should be compared directly. Unfortunately, the small number of transitions observed in this work makes it difficult to constrain the column densities accurately. Two or more transitions of a single molecule are needed to solve for the optical depth, excitation temperature and column density. We have been able to determine the column densities of thermal CH_3CN and CH_3OH through the rotational diagram method, and by assuming an excitation temperature or $^{12}\text{C}/^{13}\text{C}$ abundance ratio, we have calculated the column densities of N_2H^+ and HCO^+ . Here, we compare the beam-averaged column densities of these molecules directly to find the abundance ratios.

Lastly, we contrast the differences in a suite of measured physical parameters such as bolometric luminosity, gas mass, rotational temperature and mid-IR flux density, drawn from this and other work.

The important differences are summarized in Section 6.4.

6.1 Radio-loud versus radio-quiet sources

Fig. 10 illustrates the difference in line luminosity between sources with and without 8 GHz radio continuum emission (from UCH II regions) in the Mopra beam: the radio-loud and radio-quiet subsamples, respectively. As with CH_3CN and HCO^+ in Paper 1, we find that the luminosity of the remaining transitions is enhanced towards the radio-loud subsample. The median-line luminosity is greater by 0.65σ , on average, where σ is the standard deviation of the combined sample. Thermal CH_3OH stands out as having the most significantly different distribution and the largest difference in line luminosity, followed by H^{13}CO^+ , CH_3CN , HNC and N_2H^+ .

We find that the median linewidths of all species are broader towards the radio-loud subsample (see Fig. 11). CH_3OH exhibits

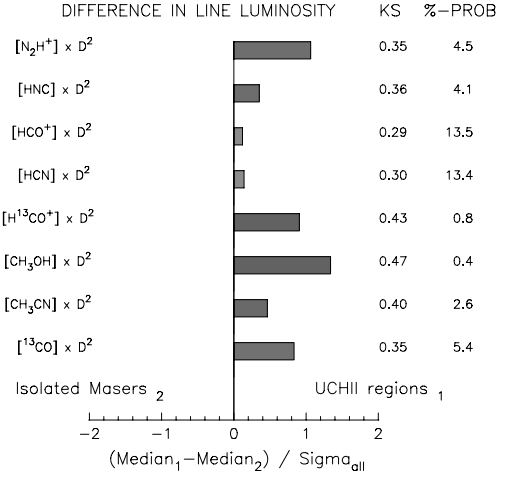


Figure 10. The bars in this horizontal histogram represent the difference between the median values of two distributions, normalized to the standard deviation of the combined sample. Here, we compare *spectral line luminosity* in sources with and without UCH II regions. A positive value means that the line is more luminous towards UCH II regions. To assess the significance of the differences, we compute the KS statistic (left-hand column) and associated percentage probability (right-hand column). As a visual aid, the grey-scale of the bars is scaled to the probability. Probabilities smaller than approximately 2 per cent (dark bars) indicate significant differences.

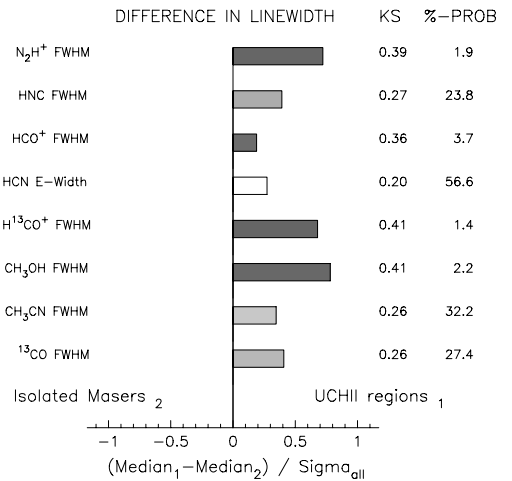


Figure 11. Differences in the median linewidth, for sources with and without an associated UCH II region. The linewidths were measured in two ways: by fitting a Gaussian to the line profile and measuring the FWHM or by integrating under the line and computing the equivalent width (HCN only). Other details are as in Fig. 10.

the greatest differences, closely followed by N_2H^+ and H^{13}CO^+ , all of which have statistically different distributions according to the KS test. HCO^+ , HCN , HNC and CH_3CN have broader lines on average; however, the distributions are not significantly different. The differences in the median linewidth between the radio-loud and radio-quiet subsample range from 0.37 to 1.62 km s $^{-1}$, greater than can be attributed to thermal broadening and most likely due to the greater turbulent energy in the gas associated with UCH II regions.

The differences found between the linewidths and line luminosities are echoed in a comparison of the raw integrated line intensities. Fig. 12 shows the difference in the median values of the 28 intensity ratios between eight molecules. The median intensity of CH_3OH and, to a lesser extent, CH_3CN is clearly enhanced

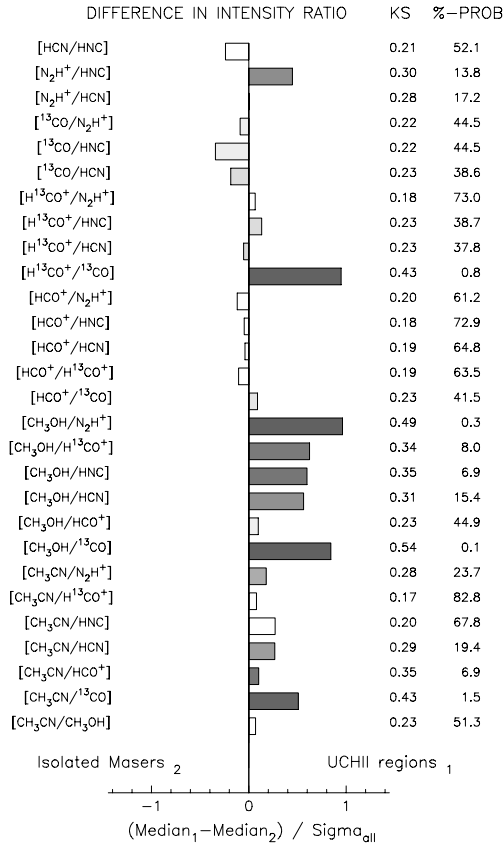


Figure 12. Differences in the median line–line intensity ratio for sources with and without an associated UCH II region. For molecules with multiple transitions (e.g. CH₃CN, CH₃OH), we have summed the intensity of all measured lines.

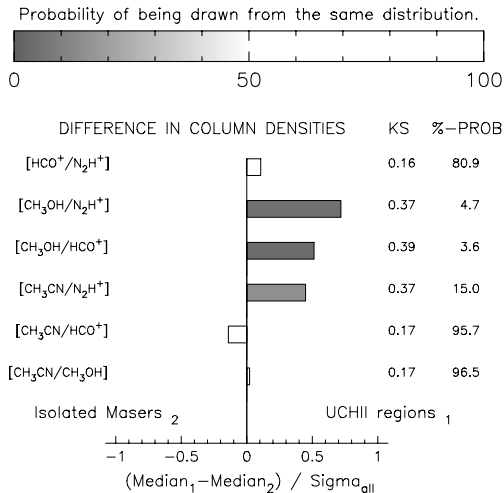


Figure 13. Differences in the median line–line column density for sources with and without an associated UCH II region.

with respect to all other molecules. Statistically, the most significant difference in intensity ratio occurs between CH₃OH and other molecules, specifically N₂H⁺ and ¹³CO. The [CH₃CN/¹³CO] and [H¹³CO⁺/¹³CO] ratios also stand out as being significantly greater towards the radio-loud subsample.

Fig. 13 illustrates a comparison of the median beam-averaged column densities of four molecules: CH₃CN, CH₃OH, HCO⁺ and

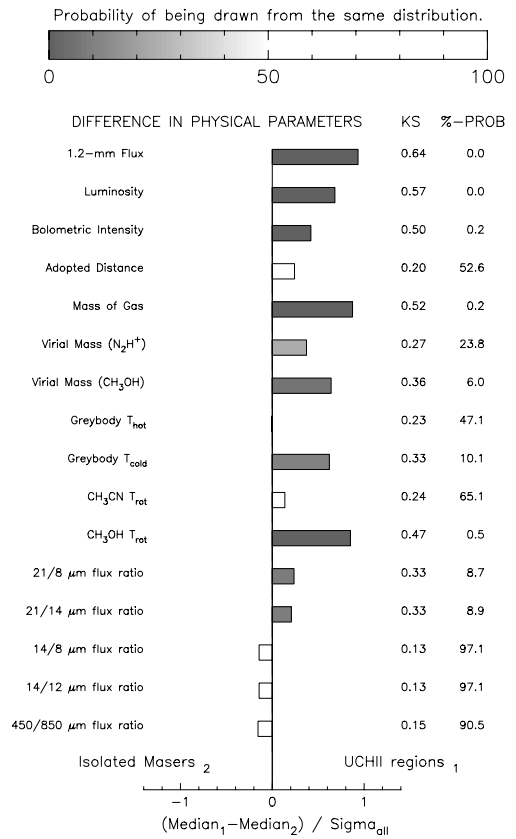


Figure 14. Differences in other computed and measured parameters for sources with and without an associated UCH II region.

N₂H⁺. Again, thermal CH₃OH stands out as having a greater column density, and hence a higher abundance, towards the radio-loud subsample.

The median differences between other measured and calculated properties are shown in Fig. 14. The median bolometric luminosity and median mass of the radio-loud subsample are significantly greater than for the isolated masers (see Section 5). The rotational temperature derived from CH₃CN is similar in both groups, however, the CH₃OH rotational temperature is significantly greater in the radio-bright group (also see Fig. 8).

6.2 Sources with and without CH₃CN

CH₃CN was detected towards 58 sources (70 per cent), however the detection rate towards the radio-loud subsample (19 sources) was 90 per cent. The enhanced luminosities and masses of our UCH II regions may bias the results of a comparison between CH₃CN-bright and CH₃CN-dark groups. We therefore exclude any regions with radio emission from the comparison. In practise, we find that the major results are robust to the presence of UCH II regions.

The differences in median line luminosity between the two groups presented in Fig. 15 are not as pronounced as in the previous section, however, all lines are marginally (0.07σ) more luminous towards the CH₃CN-bright subsample. HCO⁺ and HCN have the most significantly different distributions. We note that the HCO⁺ and HCN profiles are affected by self-absorption, with the CH₃CN-bright group containing the most extreme examples. The significant difference in the HCO⁺ luminosity is also not reflected in the optically thin H¹³CO⁺ isotopomer, suggesting that an abundance difference

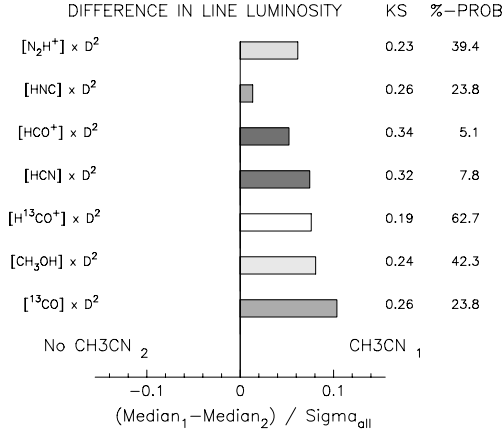


Figure 15. Differences in the median line luminosity for sources with and without CH_3CN .

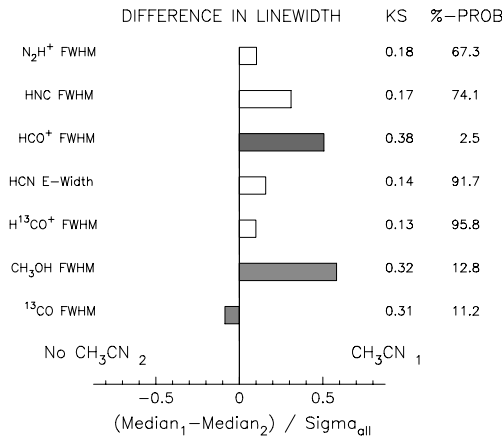


Figure 16. Differences in the median linewidth for sources with and without CH_3CN .

is unlikely. The greatest difference in the median values occurs in ^{13}CO , followed by CH_3OH and $H^{13}CO^+$.

Linewidths are also biased towards being greater in the sample with detected CH_3CN (see Fig. 16). HCO^+ exhibits the most significant difference, followed by CH_3OH , although a KS test cannot distinguish between the populations with confidence.

When we examine the line intensity ratios in Fig. 17, a similar picture emerges to the case of the UCH II regions. Thermal CH_3OH stands out, as its intensity relative to all other lines is enhanced in the CH_3CN -bright subsample. We also see evidence for enhanced N_2H^+ emission. In contrast, ^{13}CO emission is relatively weak towards the CH_3CN -bright subsample. These ratios are highly suggestive of different environmental conditions in the dense gas (traced by N_2H^+ and CH_3OH), compared to the more extended gas (traced by ^{13}CO), and correlate well with the line luminosities.

Fig. 18 shows the differences in the median column densities of CH_3OH , HCO^+ and N_2H^+ . Again, the thermal CH_3OH column is seen to be significantly enhanced towards the CH_3CN bright group, echoing the result from comparing the raw-line ratios.

The difference in the median values of other derived parameters is displayed in Fig. 20. Sources with detected CH_3CN have significantly brighter thermal continuum emission at 1.2-mm wavelengths. This translates into a mean mass higher by $\sim 300 M_\odot$, omitting UCH II regions or $\sim 600 M_\odot$, including UCH II regions.

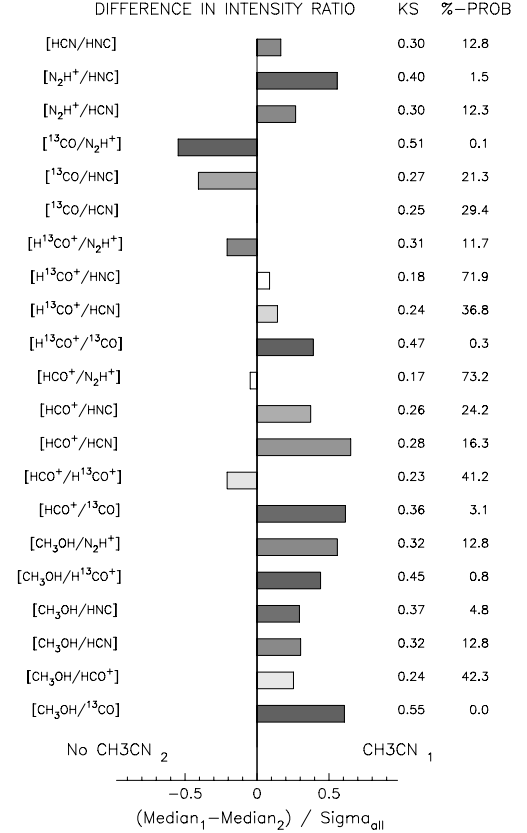


Figure 17. Differences in the median line-line intensity ratio for sources with and without CH_3CN . For line with multiple transitions, we summed the integrated intensity of all measured lines.

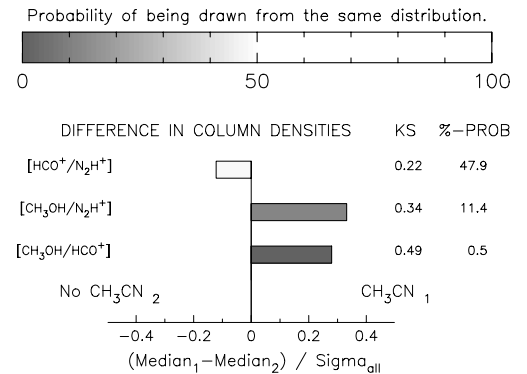


Figure 18. Differences in the median column densities for sources with and without CH_3CN .

Histograms of the mass distributions for the two groups are plotted in Fig. 19 (left-hand panel), and show significant differences. All other parameters presented in Fig. 20 are similar for both subsamples.

The division of the sample into populations with and without detected CH_3CN may be a somewhat artificial distinction. While CH_3CN emission may be present in more distant sources, it may fall below our 2σ detection threshold of 80 mK. Emission over a small solid angle will suffer from high beam dilution factors, further compounding the problem. The distributions of distance in the two samples, plotted in Fig. 19 (right-hand panel), are similar, except for a tail of more distant objects without CH_3CN . This difference

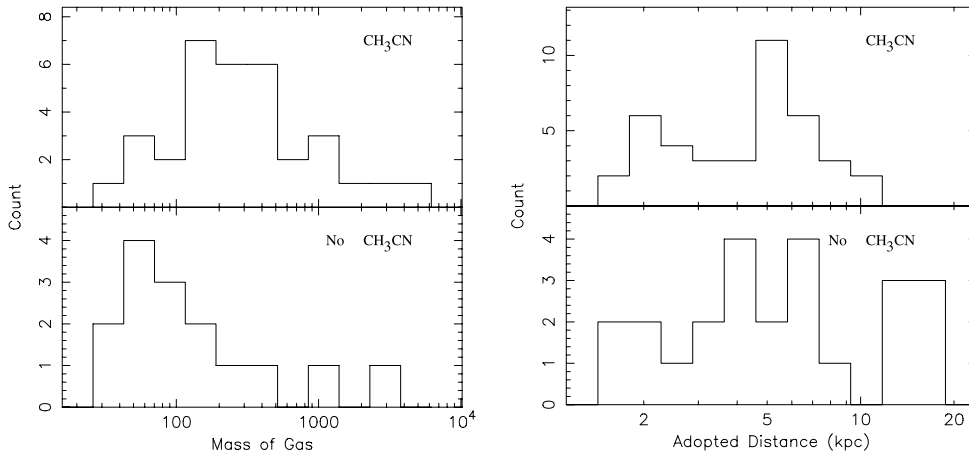


Figure 19. Left-hand panel: histograms showing the distributions of gas masses derived from 1.2-mm continuum flux density for sources with (top panel) and without (bottom panel) detected CH_3CN . Sources in which CH_3CN has been detected tend to be more massive. Right-hand panel: the distribution of distances for sources with (top panel) and without (bottom panel) detected CH_3CN . A tail of more distant objects exists in the CH_3CN -dark sample, suggesting that a small fraction of non-detections may be due to sensitivity limits.

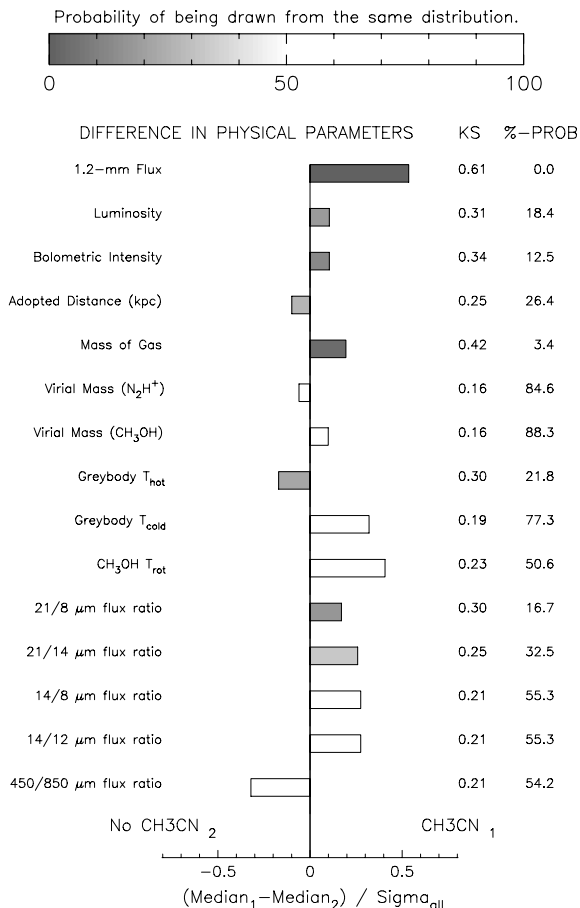


Figure 20. Differences in other computed and measured parameters for sources with and without CH_3CN .

suggests that a small fraction of non-detections may be attributable to sensitivity limits.

We also split the sample via other criteria (see the Introduction to this section), however, the chemical and physical differences are not as significant. The results of these investigations are presented as an online supplement.

6.3 The effect of beam dilution

As mentioned in Section 4.6, the beam filling factors constitute an unknown source of error when comparing the intensities or column densities of two molecules. If both emitting regions subtend angles (θ) smaller than the beam, then we must correct for the relative volume filling factor given by $(\theta_1/\theta_2)^2$. Assuming the emitting regions have similar characteristic sizes in all sources, the relative beam filling factors will average to ~ 1 over the entire sample. However, if one species generally fills the beam while the other species is generally beam-diluted (i.e. one has constant angular size while the other does not, then we would expect a $1/\text{distance}^2$ dependence in the line intensity ratios). Fig. 21 presents two plots of line intensity ratio versus distance. The left-hand panel plots the $\text{CH}_3\text{CN}/\text{CH}_3\text{OH}$ ratio versus distance. The emission from both molecules is expected to derive from regions smaller than the 36 arcsec Mopra beam, even for nearby sources. We see the line ratios are not correlated with distance, consistent with a constant ratio between the angular sizes of the species. The right-hand panel plots the $\text{CH}_3\text{CN}/\text{N}_2\text{H}^+$ ratio versus distance. Assuming N_2H^+ emission closely follows the dust morphology (e.g. Caselli et al. 2002a; Pirogov et al. 2003), we have shown in Table S9 that the beam dilution factor is generally close to 1. In Fig. 21 (right-hand panel), the dashed line plots the expected effect of CH_3CN beam dilution as a source is moved further away. We see the scatter in measured line ratio increases with distance making it difficult to interpret the data and, in addition to beam dilution, chemical and physical differences in the sources affect the line intensity ratios. Omitting the UCH II regions (squares) and considering only isolated masers (crosses), we see a possible trend towards decreasing $\text{CH}_3\text{CN}/\text{N}_2\text{H}^+$ ratio with increasing distance. This trend does not approach the $1/\text{distance}^2$ dependence expected, but it may indicate that some of our comparisons will include beam dilution effects for CH_3CN .

6.4 Interpretation and discussion

It is clear we are seeing significant differences between sources associated with different tracers. In this section, we summarize the differences between the subsamples and suggest some possible interpretations of the results.

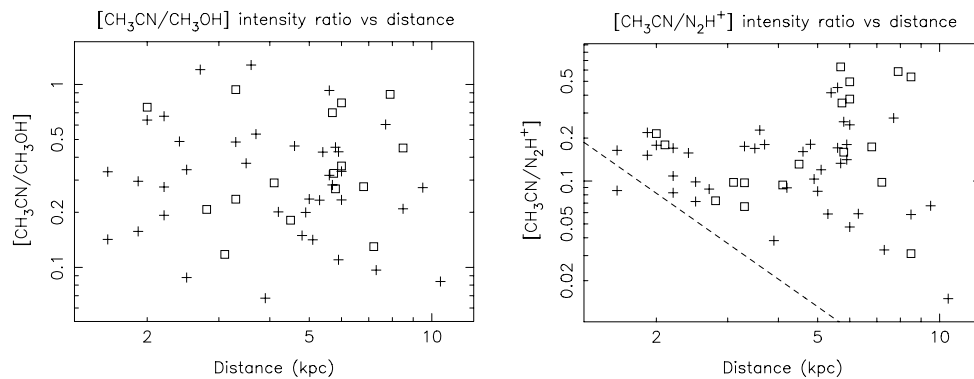


Figure 21. Plots of line–line intensity ratio versus distance. (left-hand panel) $[\text{CH}_3\text{CN}/\text{CH}_3\text{OH}]$ ratio versus distance. (right-hand panel) $[\text{CH}_3\text{CN}/\text{N}_2\text{H}^+]$ ratio versus distance. Crosses mark isolated masers, while squares mark UCH II regions. The dotted line shows how the $[\text{CH}_3\text{CN}/\text{N}_2\text{H}^+]$ ratio is expected to decrease with distance if the CH_3CN emission has a fixed physical size and the N_2H^+ emission always fills the beam.

6.4.1 UCH II regions versus isolated masers

The clearest distinctions exist between isolated CH_3OH masers and those with UCH II regions. The result found in Paper 1, where the CH_3CN and HCO^+ lines were shown to be more luminous and have greater linewidths in the presence of a UCH II region, has been extended to the other observed species. When we examine the raw line intensity ratios, thermal CH_3OH distinguishes itself as being relatively intense towards the radio-loud sources. This is reflected in both the higher median column density and CH_3OH rotational temperature. We interpret this result as evidence for an enhanced abundance of CH_3OH in relatively warm gas nearby the UCH II regions. Significant differences are also found between other tracers of high- and low-density gas. The $[\text{CH}_3\text{CN}/^{13}\text{CO}]$, $[\text{N}_2\text{H}^+/\text{CO}]$ and $[\text{H}^{13}\text{CO}^+/\text{CO}]$ ratios are enhanced in the radio-loud subsample, possibly indicating different excitation conditions or abundances in the ‘core’ compared to the ‘envelope’ gas. Interestingly, when compared to all other lines, the relative brightness of the hot-core tracer CH_3CN is *not* significantly greater, yet we detect it towards 95 per cent of UCH II regions and only 63 per cent of the isolated masers.

A potential explanation for the median offset in line luminosity and linewidths between the radio-quiet and radio-loud samples may be found in the significantly greater bolometric luminosity and gas mass of the radio-loud sample. Simply put, more luminous clumps will likely have a greater flux of IR-photons and higher gas temperatures. Under these conditions, one would expect to see more luminous spectral lines. Linewidth is commonly used as a proxy for star formation activity, and hence evolutionary state, as it is largely dependent on turbulence in massive star-forming regions. However, on the scale of molecular clouds (3–20 pc), the linewidth has also been empirically correlated with the cloud mass (Solomon et al. 1987), possibly due to multiple (sub)clumps with different velocities within the beam. It is unclear which effect dominates in our sample. Fig. 22 plots the linewidth N_2H^+ versus the gas mass. N_2H^+ is chosen as it is optically thin and has been shown to trace the dense regions of the molecular clouds (e.g. Caselli et al. 2002b). A weak correlation is observed which may account for some of the linewidth differences between the groups, however we cannot rule out an evolutionary effect.

That the relative intensity and abundance of CH_3OH is greater towards the radio-loud sources likely reflects real chemical differences between the subsamples. This may be interpreted as evidence for the more advanced evolutionary state of the radio-loud sample.

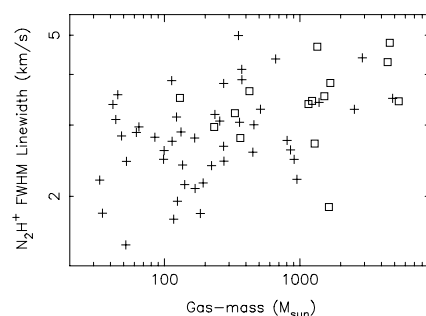


Figure 22. Plot of N_2H^+ FWHM linewidth versus gas mass. The squares represent UCH II regions and crosses represent isolated masers.

The CH_3OH abundance is predicted to be enhanced by a number of mechanisms as a massive young stellar object evolves. In the hot-core phase, it is known to be evaporated from the dust grains as the heating source evolves (Charnley et al. 1995). The abundance of CH_3OH is also predicted to be enhanced in the walls of outflow cavities, where it is sputtered from the grains by low-velocity shocks (Hogerheijde 2005).

6.4.2 CH_3CN bright versus CH_3CN dark

In this and the remaining comparisons, we removed the radio-loud sources from the list, as their higher intrinsic luminosities may bias the results. We find sources with detected CH_3CN are also biased towards having greater line luminosities and linewidths, although these differences are not as pronounced as with the radio-loud versus radio-quiet division. The most striking result is the significant tendency for thermal CH_3OH to be brighter and have a greater column density in the CH_3CN bright group. This is not unexpected as the CH_3CN and CH_3OH abundances are predicted to increase with time in hot cores (Charnley et al. 1995). We also see evidence for more turbulent and energetic conditions in the dense gas (traced by N_2H^+ and CH_3OH) compared to more extended and diffuse gas (traced by ^{13}CO), implying a more advanced evolutionary state in the CH_3CN -bright subsample. Interestingly, the CH_3CN -bright subsample also has a significantly greater median mass, which may bias this result. CH_3CN is also not detected in sources with distances greater than 10 kpc, suggesting that a small number of sources may contain CH_3CN below the sensitivity limit of our survey.

6.4.3 MSX bright versus MSX dark

All species in the MSX-dark sample have marginally greater line luminosities and linewidths compared to their MSX-bright counterparts, with the ^{13}CO linewidth being especially notable. This is unexpected, as IR dark clouds have been postulated to be the young and quiescent precursors to hot cores and UCH II regions (Rathborne, Jackson & Simon 2006). HCO^+ and CH_3OH tend to be brighter and CH_3OH marginally more abundant in the MSX-dark subsample, although this is not judged to be significant. Other parameters are similar in both subsamples. Given the small number of sources in the MSX-bright subsample (9–11 sources), none of the observed differences is large enough to draw any definite conclusions from the data.

6.4.4 Line wings versus no line wings

There are no significant differences between the median line luminosities when the sources are divided into subsamples with and without high-velocity line wings. Differences between the HCO^+ linewidth distributions can be attributed to unidentified low-velocity line wings. ^{13}CO is significantly brighter (relative to other lines) in the sources without line wings and CH_3CN is biased towards being brighter and more abundant in the subsample with line wings. No distinguishing differences are seen in the physical parameters or IR-colour ratios.

6.4.5 Infall profiles versus no infall profiles

The properties of sources with and without HCO^+ ‘infall profiles’ are close to identical. Little difference is seen between the median line luminosities, linewidths or line intensity ratios. Biases in the H^{13}CO^+ and HCO^+ line ratios can be attributed to selection effects.

The online material contains additional discussion and figures pertaining to the previous three paragraphs.

6.5 Further discussion

Is the mass of the hot core related to the dust mass? Fig. 23 shows a plot of CH_3CN beam-averaged column density versus mass of gas derived from 1.2-mm continuum emission. A clear positive correlation is seen between the two. If we assume the column of CH_3CN is a proxy for the mass of the hot core, then it follows that the mass of the hot core increases with the mass of the extended clump. The relationship is well fit by $M_{\text{CH}_3\text{CN}} \propto M_{\text{dust}}^{0.5}$ and assuming the density is constant within the gas, this implies that $M_{\text{hot core}} \propto M_{\text{dust}}^{0.5}$. This is consistent with the results of Cesaroni (2005) who found that the hot core is an continuation of the clump, and there is no break in the approximately $1/r^2$ density power law. Rather, the

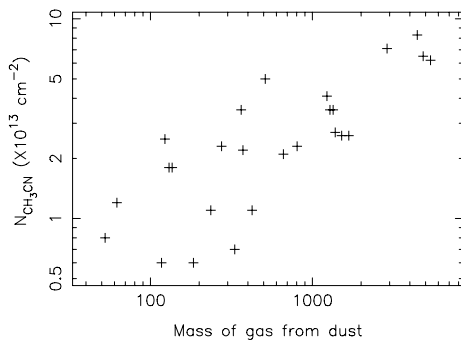


Figure 23. Plot of CH_3CN column density versus gas mass derived from 1.2-mm continuum flux density.

hot core is differentiated by temperature and excitation conditions influenced by the central heating source.

7 SUMMARY AND CONCLUSIONS

In continuation of the ‘Hot Molecular Cores’ survey, we used the Mopra telescope to search for 3-mm transitions of CH_3OH (2–1), N_2H^+ (1–0), ^{13}CO (1–0), HCN (1–0) and HNC (1–0). This is in addition to the previously reported measurements of HCO^+ (1–0), H^{13}CO^+ (1–0) and CH_3CN (5–4) and (6–5), in Paper 1. Molecular emission was detected in all but one source (G10.10–0.72), with N_2H^+ , ^{13}CO , HNC and HCN detected towards all of the remaining 82 targets. Thermal CH_3OH emission was detected in 78 sources (94 per cent). The following conclusions have been drawn from the data.

(i) Virial masses estimated from N_2H^+ are comparable to or lower than the gas masses of the sample. Values for M_{gas} have been calculated from the 1.2-mm dust emission and range from 30 to $5 \times 10^3 M_{\odot}$, while values for M_{virial} range from ~ 40 to $2.5 \times 10^3 M_{\odot}$. We note that N_2H^+ exhibits particularly narrow linewidths with an average of 3.0 km s^{-1} .

(ii) H_2 volume densities have also been estimated from the surface brightness and extent of 1.2-mm emission. The mean value is $5 \times 10^4 \text{ cm}^{-3}$, however, we note that the assumptions inherent in the calculation introduce large unknown uncertainties in the values for individual sources.

(iii) Rotational temperatures derived from CH_3OH range from 3.0 to 14.0 K , with a mean value of 6.67 K . These anomalously low temperatures strongly suggest that the CH_3OH is subthermally excited. Assuming a common excitation temperature, we find that the abundance ratio of A- to E-type CH_3OH ranges from 0.5 to 2.8 , with a mean of 1.5 , consistent with previously published values.

(iv) N_2H^+ is found to be optically thin towards most of the sample. Likewise the CH_3OH rotational diagrams are consistent with low optical depths in the $J = 2-1$ transitions. ^{13}CO , HCN and HNC all exhibit line profile asymmetries and may be significantly optically thick.

(v) The luminosity/gas-mass relationship for the sample is found to follow a rough power law of the form $L \propto M^{0.68}$, meaning that the lower mass clumps are overluminous and the higher mass clumps are underluminous. We find that the gas mass of the clumps is comparable to or greater than the mass of the stellar content (implied by the luminosity). We interpret this as an indicator of young ages, as the newborn massive stars still retain their natal molecular clouds.

(vi) The radio-loud subsample (UCH II regions) is on average more massive and more luminous than the radio-quiet subsample (isolated masers). We argue that the most likely explanation for this disparity is due to the comparatively rapid time-scale over which the most massive objects evolve into H II regions. The first significant tracer of star formation in these objects may be radio-continuum emission from a HCH II or UCH II region. It is also possible that some of the isolated maser sample contains HCH II regions which are too optically thick to detect at 8 GHz . In either case, there is a clear age difference between the subsamples.

(vii) We separated the source list into subsamples associated with different tracers of evolution and compared their median physical and chemical properties. Our findings are as follows.

(a) All spectral lines are brighter and more luminous towards the radio-loud sample, extending the result found in Paper 1.

(b) The thermal CH_3OH brightness and abundance is found to be enhanced (compared to other species) in radio-loud and CH_3CN -bright sources. We suggest that in single-dish

observations, thermal CH₃OH may be used as a crude molecular clock to indicate the evolutionary state of a clump.

(c) Given the small sample size, conclusions drawn from a comparison of MSX-bright and MSX-dark sources are not significant. It is worth noting, however, that linewidths and line luminosities are generally greater in the IR dark clouds, indicating perhaps that when selected using CH₃OH masers, dark clouds conceal objects at later stages of evolution.

(d) We divided the source list into subsamples with and without high-velocity line wings and HCO⁺-infall profiles, but found no significant differences in chemical or physical properties.

(viii) We find that the beam-averaged CH₃CN column density is correlated with the gas mass derived from 1.2-mm emission. This suggests that the mass of the hot core is dependent on the mass of the clump in which it is embedded.

ACKNOWLEDGMENTS

The authors are grateful to the Australian Research Council and UNSW for grant support. CRP and SNL were supported by a University of New South Wales School of Physics Scholarship during the course of this research. The Mopra radio telescope is part of the Australia Telescope which is funded by the Commonwealth of Australia for operations as a National Facility managed by CSIRO. During 2002–2005, the Mopra telescope was operated through a collaborative arrangement between the University of New South Wales and the CSIRO.

This research has made use of NASA's Astrophysics Data System.

We would also like to thank the anonymous referee for being especially thorough in seeking out mistakes in the paper. His/her comments were extremely useful and have helped to improve the presentation and interpretation.

REFERENCES

- Allen C. W., 1973, *Astrophysical Quantities*, 3rd edn. University of London, Athlone Press, London
- Avalos M., Lizano S., Rodríguez L. F., Franco-Hernández R., Moran J. M., 2006, *ApJ*, 641, 406
- Blake G. A., Masson C. R., Phillips T. G., Sutton E. C., 1986, *ApJS*, 60, 357
- Bockelée-Morvan D., Crovisier J., Colom P., Despois D., 1994, *A&A*, 287, 647
- Brand J., Blitz L., 1993, *A&A*, 275, 67
- Caselli P., Myers P. C., Thaddeus P., 1995, *ApJ*, 455, L77
- Caselli P., Benson P. J., Myers P. C., Tafalla M., 2002a, *ApJ*, 572, 238
- Caselli P., Walmsley C. M., Zucconi A., Tafalla M., Dore L., Myers P. C., 2002b, *ApJ*, 565, 331
- Cesaroni R., 2005, in Cesaroni R., Felli M., Churchwell E., Walmsley M., eds, *Proc. IAU Symp.*, Vol. 227, *Hot Molecular Cores*, p. 59
- Cesaroni R., Neri R., Olmi L., Testi L., Walmsley C. M., Hofner P., 2005, *A&A*, 434, 1039
- Charnley S. B., Kress M. E., Tielens A. G. G. M., Millar T. J., 1995, *ApJ*, 448, 232
- Churchwell E., 2002, *ARA&A*, 40, 27
- Cummins S. E., Linke R. A., Thaddeus P., 1986, *ApJS*, 60, 819
- Dobbs C. L., Bonnell I. A., Clark P. C., 2005, *MNRAS*, 360, 2
- Doty S. D., van Dishoeck E. F., van der Tak F. F. S., Boonman A. M. S., 2002, *A&A*, 389, 446
- Estalella R., Mauersberger R., Torrelles J. M., Anglada G., Gomez J. F., Lopez R., Muters D., 1993, *ApJ*, 419, 698
- Goldsmith P. F., Langer W. D., 1999, *ApJ*, 517, 209
- Hildebrand R. H., 1983, *QJRAS*, 24, 267
- Hill T., Burton M. G., Thompson M. A., Walsh A. J., Hunt-Cunningham M., Garay G., 2005, *MNRAS*, 363, 405
- Hoare M. G., Lumsden S. L., Oudmaijer R. D., Busfield A. L., King T. L., Moore T. L. J., 2004, in Clemens D., Shah R., Brainerd T., eds, *ASP Conf. Ser.*, Vol. 317, *Milky Way Surveys: The Structure and Evolution of our Galaxy*. Astron. Soc. Pac., San Francisco, p. 156
- Hogerheijde M. R., 2005, *Ap&SS*, 295, 179
- Kim H.-D., Cho S.-H., Chung H.-S., Kim H.-R., Roh D.-G., Kim H.-G., Minh Y. C., Minn Y.-K., 2000, *ApJS*, 131, 483
- Kim H.-D., Cho S.-H., Lee C.-W., Burton M. G., 2001, *J. Korean Astron. Soc.*, 34, 167
- Kim H.-D., Balasubramanyam R., Burton M. G., 2002, *Publ. Astron. Soc. Aust.*, 19, 505
- Kurtz S., Churchwell E., Wood D. O. S., 1994, *ApJS*, 91, 659
- Kurtz S., Cesaroni R., Churchwell E., Hofner P., Walmsley C. M., 2000, in Mannings V., Boss A. P., Russell S. S., eds, *Protostars and Planets IV*. University of Arizona Press, Tucson, p. 299
- Lada C. J., 1999, in Lada C. J., Kylafis N. D., eds, *NATO ASIC Proc. 540: The Origin of Stars and Planetary Systems*. Dordrecht, Kluwer, p. 143
- Longmore S. M., Burton M. G., Barnes P. J., Wong T., Purcell C. R., Ott J., 2007, *MNRAS*, 379, 535
- MacDonald G. H., Gibb A. G., Habing R. J., Millar T. J., 1996, *A&AS*, 119, 333
- MacLaren I., Richardson K. M., Wolfendale A. W., 1988, *ApJ*, 333, 821
- Menten K. M., Walmsley C. M., Henkel C., Wilson T. L., 1988, *A&A*, 198, 253
- Millar T. J., MacDonald G. H., Gibb A. G., 1997, *A&A*, 325, 1163
- Mottram J., 2008, PhD thesis, Univ. Leeds
- Ossenkopf V., Henning T., 1994, *A&A*, 291, 943
- Pickett H. M., Poynter R. L., Cohen E. A., Delitsky M. L., Pearson J. C., Muller H. S. P., 1998, *J. Quant. Spectrosc. Radiat. Transfer*, 60, 883
- Pirogov L., Zinchenko I., Caselli P., Johansson L. E. B., Myers P. C., 2003, *A&A*, 405, 639
- Purcell C. R., 2006, *MNRAS*, 371, 799
- Rathborne J. M., Jackson J. M., Simon R., 2006, *ApJ*, 641, 389
- Rodgers S. D., Charnley S. B., 2003, *ApJ*, 585, 355
- Rohlfs K., Wilson T. L., 2004, in Rohlfs K., Wilson T. L., eds, *Tools of Radio Astronomy*. Springer, Berlin, p. 379
- Schilke P., Groesbeck T. D., Blake G. A., Phillips T. G., 1997, *ApJS*, 108, 301
- Schilke P., Walmsley C. M., Pineau Des Forets G., Roueff E., Flower D. R., Guilloteau S., 1992, *A&A*, 256, 595
- Solomon P. M., Rivolo A. R., Barrett J., Yahil A., 1987, *ApJ*, 319, 730
- Sutton E. C., Jaminet P. A., Danchi W. C., Blake G. A., 1991, *ApJS*, 77, 255
- Thompson M. A., MacDonald G. H., Millar T. J., 1999, *A&A*, 342, 809
- Townes C. H., Schawlow A. L., 1955, *Microwave Spectroscopy*. McGraw Hill, New York
- Turner B. E., 1989, *ApJS*, 70, 539
- Walsh A. J., Burton M. G., 2006, *MNRAS*, 365, 321
- Walsh A. J., Hyland A. R., Robinson G., Burton M. G., 1997, *MNRAS*, 291, 261
- Walsh A. J., Burton M. G., Hyland A. R., Robinson G., 1998, *MNRAS*, 301, 640
- Walsh A. J., Macdonald G. H., Alvey N. D. S., Burton M. G., Lee J.-K., 2003, *A&A*, 410, 597
- Weidner C., Kroupa P., 2004, *MNRAS*, 348, 187
- Ziurys L. M., McGonagle D., 1993, *ApJS*, 89, 155

SUPPORTING INFORMATION

Additional Supporting Information may be found in the online version of this article.

Appendix A. Maser-selected hot cores and UCH II Regions.

Please note: Wiley-Blackwell are not responsible for the content or functionality of any supporting materials supplied by the authors. Any queries (other than missing material) should be directed to the corresponding author for the article.

This paper has been typeset from a \LaTeX file prepared by the author.